

Iron (Fe) speciation in size-fractionated aerosol particles in the Pacific Ocean: The role of organic complexation of Fe with humic-like substances in controlling Fe solubility

5 Kohei Sakata¹, Minako Kurisu², Yasuo Takeichi³, Aya Sakaguchi⁴, Hiroshi Tanimoto¹, Yusuke Tamenori⁵, Atsushi Matsuki⁶, Yoshio Takahashi^{3,7}

¹Center for Global Environmental Research, National Institute for Environmental Studies, 16-2 Onogawa, Tsukuba, Ibaraki 305-8506, Japan.

²Research Institute for Global Change, Japan Agency for Marine-Earth Science and Technology, 2-15, Natsushima-cho, Yokosuka, Kanagawa 237-0061, Japan.

10 ³Institute of Materials Structure Science, High-Energy Accelerator Research Organization, Tsukuba, Ibaraki 305-0801, Japan.

⁴Faculty of Pure and Applied Science, University of Tsukuba, 1-1-1 Tennodai, Tsukuba, Ibaraki 305-8577, Japan.

⁵Japan Synchrotron Radiation Research Institute/SPring-8, 1-1-1 Kouto, Sayo, Hyogo 679-5198, Japan.

⁶Institute of Nature and Environmental Technology, Kanazawa University, Kakuma, Kanazawa, Ishikawa 920-1192, Japan.

⁷Graduate School of Science, The University of Tokyo, 7-3-1 Hongo, Bunkyo-ku, Tokyo 113-0033, Japan.

15 *Correspondence to:* Kohei Sakata (sakata.kohei@nies.go.jp)

~~Abstract:~~
Abstract

20 Atmospheric deposition is one of the ~~dominant~~main sources of dissolved Fe ~~en~~in the ocean ~~surfaces~~surfaces. Atmospheric processes are recognized as controlling fractional Fe solubility ($Fe_{sol}\%$) in marine aerosol particles, ~~but~~. However, the impact of these processes on $Fe_{sol}\%$ remains unclear. One of the reasons for this is the lack of field observations focusing on the relationship between $Fe_{sol}\%$ and Fe species in ~~the~~ marine aerosol particles. In particular, the effects of organic ligands on ~~the~~ $Fe_{sol}\%$ have not been well~~thoroughly~~ investigated through~~in~~ observational studies. In this study, Fe species in size-fractionated aerosol particles in the Pacific Ocean were determined by~~using~~ X-ray absorption fine structure (XAFS) spectroscopy. The internal mixing states of Fe ~~with~~and organic ~~carbons~~carbon were investigated using scanning transmission X-ray microscopy (STXM). The effects of atmospheric processes on $Fe_{sol}\%$ in ~~the~~ marine aerosol particles were investigated based on ~~these~~the speciation results. Iron in size-fractionated aerosol particles was mainly derived from mineral dust, regardless of aerosol diameter, because the enrichment factor of Fe was almost 1 in both coarse (~~$PM_{1.3-10.2}$~~) and fine aerosol particles ($PM_{1.3}$). ~~About~~Approximately 80% of ~~the~~ total Fe (insoluble + labile Fe) was present in ~~coarse aerosol particles ($PM_{1.3-10.2}$)~~, whereas labile Fe was mainly present in ~~fine aerosol particles ($PM_{1.3}$)~~. The $Fe_{sol}\%$ in ~~$PM_{1.3-10.2}$~~ was not well~~significantly~~ increased ($2.56 \pm 2.53\%$, 0.00–8.50%, n = 20) by the atmospheric processes because mineral dust was not acidified beyond the buffer capacity of calcite. By~~In~~ contrast, mineral dust in $PM_{1.3}$ was acidified beyond the buffer capacity of calcite. As a result, $Fe_{sol}\%$ in $PM_{1.3}$ (0.202–64.7%, n = 10) ~~is~~was an order of magnitude higher than ~~those~~that in ~~$PM_{1.3-10.2}$~~ . The $PM_{1.3}$ contained ferric organic complexes with humic-like substances (Fe(III)-HULIS, but not ~~included~~ Fe-oxalate complexes), ~~of which~~whose abundance correlated with $Fe_{sol}\%$. ~~The Fe~~Iron(III)-HULIS was formed during transport in the Pacific Ocean ~~since~~ ~~the~~because Fe(III)-HULIS was not found in aerosol particles in Beijing and Japan. The pH estimations of mineral dust in $PM_{1.3}$ ~~revealed~~established that Fe was solubilized by proton-promoted dissolution under highly acidic conditions (pH < 3.0), whereas Fe(III)-HULIS was stabilized under moderately acidic conditions (pH = 3.0–6.0). Since the observed labile Fe concentration could not be reproduced by proton-promoted dissolution under moderately acidic conditions, the pH of mineral dust ~~was~~ increased after proton-promoted dissolution. The cloud process in the marine atmosphere ~~increased~~increases the ~~pH of~~ mineral dust pH because the dust particles ~~were~~are covered with organic ~~carbons~~carbon and Na. ~~At this stage, the~~The precipitation of ferrihydrite was suppressed by Fe(III)-HULIS ~~because of~~owing to its high water solubility. Thus, the organic complexation of Fe with HULIS plays a significant role in the stabilization of Fe ~~that~~ was initially solubilized by proton-promoted dissolution.

45 1. Introduction

Primary production on the ocean surface is limited by the depletion of dissolved iron (Fe, Martin and Fitzwater, 1988; Jickells et al., 2005; Baker et al., 2016, 2021; Mahowald et al., 2018; Meskhidze et al., 2019). The fertilization of Fe in the surface ocean has the potential to regulate global climate systems ~~via~~through the uptake of atmospheric carbon ~~dioxides~~dioxide (CO₂) in ~~the~~ surface seawater. Dissolved ~~iron~~Fe must be supplied to activate biological activity because 50 microorganisms utilize dissolved Fe as ~~micronutrients~~a micronutrient (Boyd et al., 2007; Moore et al., 2013; Mahowald et al., 2018). Atmospheric deposition of Fe in mineral dust is ~~one of the~~ dominant ~~source~~source of dissolved Fe on the ocean surface (Jickells et al., 2005; Baker et al., 2016, 2021; Mahowald et al., 2018; Meskhidze et al., 2019). However, fractional Fe solubility ($Fe_{sol}\% = (\text{labile Fe}/\text{total Fe}) \times 100$) in mineral dust in source regions is usually ~~less than~~below 1.0% because Fe in mineral dust is typically present as insoluble species (e.g., Fe in aluminosilicates and Fe (hydr)oxides). In contrast, a 55 wide range of $Fe_{sol}\%$ in marine aerosol particles (0.1–90%) has been reported ~~by~~in previous observational studies (Buck et al., 2006; 2010; 2013, Baker and Jickells, 2006; Bakers et al., 2016, 2021; Chance et al., 2015; Kurisu et al., 2021). One of the reasons for ~~the~~ high $Fe_{sol}\%$ in ~~the~~ marine aerosol particles is pyrogenic Fe with high $Fe_{sol}\%$ (up to 80%, Schroth et al., 2009; Takahashi et al., 2013; Kurisu et al., 2016; 2019, 2021; Conway et al., 2019). It seems that the variation ~~of~~in $Fe_{sol}\%$ in marine aerosol particles can be explained by a binary mixing system of mineral dust and anthropogenic aerosols if the $Fe_{sol}\%$ 60 of these components at the time of emission is known. However, ~~it is difficult to explain~~explaining the variation of $Fe_{sol}\%$ in ~~the~~ marine aerosol particles by the mixing system ~~is difficult~~ because atmospheric processes during transport affect ~~the~~ $Fe_{sol}\%$ of mineral dust and anthropogenic Fe.

~~Atmospheric~~The atmospheric processes of Fe are described as proton-promoted, ligand-promoted, and photo-reductive Fe dissolutions (Bakers et al., 2016, 2021; Mahowald et al., 2018; Meskhidze et al., 2019 and references therein). ~~The~~ 65 ~~proton~~Proton-promoted Fe dissolution is ~~driven~~mainly ~~driven~~by aerosol ~~acidifications~~acidification (Desboufs et al., 1999; Mackie et al., 2005; Cwiertny et al., 2008; Shi et al., 2009, 2011, 2015; Maters et al., 2016). As a proof of the acidification of Fe-bearing particles, ~~the~~ single-particle analysis revealed that internal mixing of Fe with sulfate, nitrate, and chloride ~~were~~was identified in the atmosphere (Sullivan et al., 2007; Moffet et al., 2012; Fitzgerald et al., 2015; Li et al., 2017), but these analytical techniques could not ~~mention~~establish a ~~relationships of~~relationship between ~~the~~ internal mixing state 70 ~~with~~ aerosol pH and $Fe_{sol}\%$. Therefore, aerosol pH ~~was~~is usually estimated ~~by~~using thermodynamic model calculations (e.g., E-AIM and ISOROPPIA). The ~~Fe~~ dissolution ~~of Fe~~ from aerosol particles is enhanced in the wet aerosol phase ~~with~~under highly acidic conditions (pH < 3.0, Longo et al., 2016; Fang et al., 2017; Tao and Murphy, 2019). However, ~~the pH values~~ calculated ~~pH~~by the thermodynamic models ~~does~~do not necessarily reflect the pH of the mineral dust. One of the reasons ~~for~~ ~~this~~ is that the calculated result is the pH of the main component of ~~the~~ marine aerosols (e.g., sulfate aerosols and sea spray aerosols), which ~~were~~are usually externally mixed with Fe-bearing particles. Another reason is that the aerosol pH of proton-promoted dissolution cannot uniquely determine the aerosol pH ~~since~~because the Fe-bearing particles may ~~go~~ ~~through~~undergo pH cycles according to evaporation–condensation cycles. Therefore, ~~it is preferred that~~evaluating the

average pH of Fe-bearing particles for proton-promoted dissolution ~~are evaluated~~ based on the $\text{Fe}_{\text{sol}}\%$ and/or labile (L-Fe) concentrations is appropriate.

80 In ~~the case of~~ ligand-promoted and photo-reductive Fe dissolutions, organic ligands play a significant role in ~~the enhancement of enhancing~~ $\text{Fe}_{\text{sol}}\%$ in marine aerosol particles. The formation of organic complexes on the surface of Fe-oxides destabilizes the Fe-O ~~bonds~~ (Wang et al., 2017). ~~The complexation of~~ Moreover, the formation of organic complexes with L-Fe with organic complexes decreases a saturation index of in the aqueous phase promoted further Fe ~~dissolution from the aerosol particles to~~ aerosol liquid water (ALW). The photoreduction of Fe(III)-organic complexes also
85 decreases the saturation index of Fe(III) in ~~the~~ ALW because of the formation of Fe(II) (Chen and Grassian, 2013). As a result of these interactions ~~efbetween~~ Fe ~~withand~~ organic ligands, the dissolution of Fe-bearing particles is promoted. ~~ItOxalate~~ is considered ~~that oxalate is~~ an important ligand in aerosol particles because oxalate is ubiquitously present in aerosol particles. However, the mass fraction of oxalate in water-soluble organic carbon (WSOC) is usually typically lower than 10% (Bikkina et al., 2015; Kawamura and Bikkina, 2016). In contrast, more than half of WSOC is present as humic-
90 like substances (HULIS), which are ~~also~~ considered to affects affect $\text{Fe}_{\text{sol}}\%$ in aerosol particles (Wozniak et al., 2013, 2015; Al-Abdleh 2015). Atmospheric HULIS in marine aerosols are formed by atmospheric processes and direct emissions from the ocean surface (Deng et al., 2014; Chen et al., 2016; Santander et al., 2021), whereas soil-derived organic matter is generally not an important source of atmospheric HULIS (Graber and Rudich, 2006; Spranger et al., 2020). In addition, siderophores have been detected in ~~aerosol~~ aerosols, rainwater, and cloud water, which are likely formed by biological
95 activities in mineral dust and cloud water (Cheize et al., 2012; Sullivan et al., 2012; Vinatier et al., 2016). The siderophore has a higher stability constant with Fe than with oxalate, and ~~the~~ Fe-siderophore complexes have high water solubility (Cheize et al., 2012). Recently, ~~the~~ Fe(III)-dextran as Fe(III)-organic complexes have been were detected in $\text{PM}_{2.5}$ collected in Colorado, USA (Salazar et al., 2020). The formation of Fe-organic complexes may suppress the precipitation of nano-ferrihydrate when ~~the~~ acidified aerosol particles with high $\text{Fe}_{\text{sol}}\%$ ~~encounters~~ encounter high-~~pH~~ solutions
100 because these Fe-organic complexes have higher water solubility than inorganic Fe under over a wide pH range. However, the effects of Fe(III)-organic complexes of HULIS and ~~siderophores~~ siderophores in atmospheric samples on $\text{Fe}_{\text{sol}}\%$ have not been well investigated through ~~the~~ field observations of marine aerosol particles.

~~In this~~ This was a case study, on the relationship between $\text{Fe}_{\text{sol}}\%$ and Fe species in size-fractionated aerosol particles ~~in collected from~~ the Pacific Ocean. The iron species in the aerosol samples were determined ~~by using~~ X-ray absorption fine
105 structure (XAFS) spectroscopy to investigate ~~athe~~ relationship between Fe species and $\text{Fe}_{\text{sol}}\%$. ~~The~~ XAFS spectroscopy provides ~~us~~ the average fraction of Fe species, which can be directly ~~compare~~ compared to the $\text{Fe}_{\text{sol}}\%$. In addition, ~~the~~ Al species in several size-fractionated aerosol particles were determined ~~to evaluate~~ for evaluating the aging effect of the aluminosilicates in the samples. The Al K-edge X-ray absorption near-edge structure (XANES) spectrum is sensitive to the coordination chemistry of Al (Ildefonse et al., 1998; Shaw et al., 2009; Hagvall et al., 2015). Furthermore, the internal
110 mixing states of Fe ~~withand~~ organic ~~carbons~~ carbon (OCs) were investigated using scanning transmission X-ray microscopy (STXM) ~~to evaluate~~ for evaluating the detailed alteration processes of Fe-bearing particles. Based on the $\text{Fe}_{\text{sol}}\%$ and

speciation results, the ~~average expected~~ pH required for L-Fe concentration in the aerosol samples by proton-promoted dissolution within the transport time (pH_{PPD}) was evaluated using a conceptual model ~~according to the following~~ first-order ~~Feiron~~ dissolution. ~~The~~In addition to pH_{PPD}, pH for stabilization of L-Fe species in aerosol particles (pH_{L-Fe}) was evaluated by a geochemical model. If pH_{L-Fe} differs from pH_{PPD}, ~~the~~L-Fe species are formed under different pH conditions from ~~the~~ proton-promoted ~~dissolutions~~dissolution. Therefore, ~~the~~ differences between pH_{PPD} and pH_{L-Fe} may ~~become~~be an indicator ~~for of the~~ pH variation of the Fe-bearing particles. From these results, the role of atmospheric processes ~~in the enhancement of for enhancing~~ Fe_{sol}% ~~is~~was discussed in this study.

2. Sampling and analytical methods

2.1. Aerosol sampling

Size-fractionated sampling of marine aerosols was conducted ~~enduring~~ the research cruise of *R/V Hakuho-Maru* (Fig. 1 and Table S1: KH-14-6, ~~Longitudinal~~longitudinal cruise of the ~~Western~~ Pacific Ocean, December 2, 2014, to February 26, 2015, GEOTRACES). Three size-fractionated aerosol particles were collected from the western Pacific Ocean (WPO), and one sample was collected from the central Pacific Ocean (CPO) and southern Pacific Ocean (SPO, Fig. 1). A high-volume air sampler (MODEL-123SL, Kimoto, Japan) with a Sierra-type cascade impactor (TE-236, Tisch Environmental Inc., USA) was installed on the compass deck of the vessel, located 13 m above sea level. ~~A~~The sampling ~~air flow~~airflow rate was ~~fixed~~set at 0.566 m³/min. ~~Wind~~The wind speed and direction were monitored ~~by using~~ a wind-sector control system to prevent the contamination of fly ~~ashes~~ash and exhaust gases emitted from the vessel.

~~Aerosol~~Aerosol samples were stored in a dry desiccator at 20 % relative humidity and room temperature (approximately 20 °C). Aerosol particles were collected in seven stages, of which aerodynamic diameters for each sampling were >10.2 μm (stage-1 to 7) are described in Table-1: S1. Aerosol samples in stages 1 to 4 (PM_{1.2-10.2} μm (stage-2: S2), 2.1–4.2 μm (stage-3 ~~to 2~~→: S3), 1.3–μm)–2.1 μm (stage-4: S4), 0.69–1.3 μm (stage-5: S5), 0.39–0.69 μm (stage-6: S6), and <0.39 μm (stage-7: S7). Aerosol samples in S1 to S4 were defined as coarse aerosol particles, (PM_{>1.3}), whereas those in stages ~~5S5~~ to ~~7S7~~ were defined as fine aerosol particles (PM_{1.3} < 1.3 μm). Aerosol particles in ~~stages 1 to 6~~S1–S6 were collected on a custom-built polytetrafluoroethylene (PTFE, ~~about~~, approximately 15 cm²) filter (Sakata et al. 2018). The PTFE filter was rinsed using the following procedures with heating at 150 °C: ultrapure water (MQ, Merck Millipore, USA), 3 mol/L HNO₃ (Electric grade, Kanto Chemical, Japan), 3 mol/L HCl (Electric grade, Kanto Chemical, Japan), and MQ water (Sakata et al., 2018). ~~The filter blanks of~~The Al and Fe blanks in the PTFE filter were 0.306 ± 0.352

and 0.335 ± 0.340 ng/cm², which were corresponding to respectively. The unit of the filter blank concentration was converted from ng/cm² to ng/m³ using the following equation:

$$\text{Filter blank (ng/m}^3\text{)} = \frac{\text{filter blank (ng/cm}^2\text{)} \times \text{filter area (cm}^2\text{)}}{\text{Total flow for each sampling (m}^3\text{)}} \quad (\text{Eq. 1})$$

As a result, the blank concentrations of Al and Fe were a few pg/m³. The blank concentrations of Fe and Al were ~~about~~ ~~an~~ approximately one order of magnitude lower than the lowest ~~concentration~~ concentrations of these elements in ~~our~~ the samples. For single-particle analysis, aerosol particles were ~~also~~ collected on molybdenum grids with a formvar thin film (Mo grid) ~~that~~ fixed on the PTFE filter ~~by~~ using double-face cellulose tape. ~~The PTFE filter was rinsed based on our previous study (Sakata et al., 2018).~~ Aerosol samples ~~in stage 7 from S7~~ were collected on a cellulose filter (Whatman 41, 516 cm², GE Healthcare, USA). The filter blank of Al and Fe in the cellulose filter ~~was~~ 7.20 ~~±3.91~~ and 16.5 ~~±6.27~~ ng/cm², which ~~are~~ corresponded to 2.52 and 5.77 ng/m³, respectively. Stage 7 was excluded from the discussion because of ~~theits~~ high-filter background. In this study, the sample names are described as the stage number of the cascade impactor combined with the sampling site (e.g., stage 6 collected in SPO: S6-SPO; ~~Tables S1 and S2~~).

~~For comparison, aerosol~~ Aerosol sampling was performed at the Noto Ground-~~Based~~ based Research Observatory (NOTOGRO) located in the coastal region of the Sea of Japan (Suzu, Ishikawa, Japan: ~~37.4513°~~ 4513 °N, ~~137.3589°~~ 3589 °E). NOTOGRO is located between China and the sampling sites ~~of~~ in the WPO (Fig. 1). Size-fractionated aerosol ~~samples~~ samples influenced by Chinese air ~~mass~~ masses were collected from February 19 to 26, 2020. ~~(Fig. S1a)~~. In addition, the reference ~~materials~~ material of Beijing aerosol (NIES CRM 28, Urban dust, Mori et al., 2008) was also employed for ~~comparison of~~ comparing Fe species.

2.2. Total and labile metal concentrations

All sample treatments were conducted in a clean booth (Class-100) and ~~an~~ evaporation chamber installed in a Class-10000 clean room. Acid digestion and ultrapure water ~~extraction~~ extraction of aerosol samples were performed ~~to~~ determine for determining total and labile metal concentrations, respectively. Aerosol samples were decomposed ~~by~~ using mixed acid (2 mL of 15.2 mol/L HNO₃, 2 mL of 9.3 mol/L HCl, and ~~1 mL~~ 1 mL of 20 mol/L HF) ~~with heating and heated~~ at 120 °C for 1 ~~day~~ d. The mixed acid was evaporated to dryness at 120 °C, ~~subsequently and the~~ residues were re-dissolved in 0.15 mol/L HNO₃. Labile metals in the aerosol particles were extracted ~~ultrasonically~~ ultrasonically for 30 min ~~with~~ using 5 mL of MQ water. The extracted solutions were acidified to 0.15 mol/L after filtration of insoluble particles. using a hydrophilic syringe PTFE filter (φ:0.20 μm, Dismic®, 25HP020AN, Advantec, Japan). Total and labile metal concentrations were determined ~~by~~ using inductively coupled plasma mass spectrometry (ICP-MS, Agilent 7700, Agilent, Japan). Total and labile metal concentrations in total suspended ~~particulate~~ particulates (TSP) were calculated by ~~summation of~~ summing target

metal concentrations in stages 1 to 6. ~~Fractional~~The fractional Fe and Al solubility ($Fe_{sol}\%$ and $Al_{sol}\%$, respectively) and enrichment factors (EF) were calculated using the following equations:

$$Fe_{sol}\% = (\text{labile Fe}/\text{total Fe}) \times 100 \quad \text{--- (Eq. 42)}$$

$$Al_{sol}\% = (\text{labile Al}/\text{total Al}) \times 100 \quad \text{--- (Eq. 23)}$$

$$EF = (Fe/Al)_{\text{aerosol}} / (Fe/Al)_{\text{crust.}} \quad \text{--- (Eq. 3) (Eq. 4)}$$

~~From~~The Fe and Al concentrations in the ~~average~~continental crust were ~~cited~~referred from Taylor (1964).

2.3. Major ion and ~~water-soluble organic carbon~~WSOC concentrations

~~Major~~The major ions (Na^+ , NH_4^+ , K^+ , Mg^{2+} , Ca^{2+} , Cl^- , NO_3^- , SO_4^{2-} , and $C_2O_4^{2-}$) in the aerosol samples were extracted ~~by using~~ the same methods for labile metal ~~extractions~~. ~~Water-soluble organic carbon (WSOC) was extracted using 15 mL of MQ water in glass vials on a shaker for 1 hour.~~ Major ions and WSOC extraction. The major ion concentrations were measured using ion chromatography (ICS-1100, Dionex, Japan) ~~and a total carbon analyzer (TOC-V CSH, Shimadzu, Japan)~~. The guard and separation columns for cations were Ion Pac CG12A and CS12A, respectively. ~~Detail methods, and those for ion chromatography are described in~~ anions were Ion Pac AG22 and AS22, respectively. The guard and separation ~~columns were installed in a thermo-controlled box (30 °C). The eluents for cations and anions were 20 mmol/L of methanesulfonic acid and a mixed solution of 4.5 mmol/L Na_2CO_3 /1.4 mmol/L $NaHCO_3$. After passing through the column, the eluents were passed through a suppressor and were introduced into the conductivity detector. The detection limits of the ICS-1000 for Na^+ , NH_4^+ , K^+ , Mg^{2+} , Ca^{2+} , Cl^- , NO_3^- , SO_4^{2-} , and $C_2O_4^{2-}$ were 0.556, 0.464, 1.15, 0.726, 1.50, 5.62, 15.0, 18.8, and 33.2 ng/mL, respectively. Among the targeted ions, the lowest and highest filter blank concentrations were 0.0687 and 32.4 ng/cm² for Mg^{2+} and SO_4^{2-} , respectively (Sakata et al., 2018). After the unit conversion of the filter blank from ng/cm² to ng/m³ using Equation 1, the highest filter blank concentration was 4.47 ng/m³ SO_4^{2-} . Semi-volatile compounds (e.g., NH_4NO_3) were affected by negative artifacts during sampling. The negative artifact effect was unlikely to be significant because most nitrates were present in $PM_{>1.3}$ with a small concentration of NH_4^+ . However, some NH_4NO_3 present in $PM_{1.3}$ may be affected by the negative artifact. The negative artifacts of oxalate and ammonium sulfate are usually negligible in IC analyses (Yao et al., 2002; Bian et al., 2014). ~~Non~~The non-sea- salt (nss) SO_4^{2-} and Ca^{2+} were calculated ~~by using~~ the following equation:~~

$$[nss-SO_4^{2-} \text{ or } nss-Ca^{2+}] = [SO_4^{2-} \text{ or } Ca^{2+}]_{\text{aerosol}} - [Na^+]_{\text{aerosol}} \times ([SO_4^{2-} \text{ or } Ca^{2+}]/[Na^+])_{\text{seawater}} \quad \text{--- (Eq. 45)}$$

~~To evaluate acidification degrees~~WSOC was extracted using 15 mL of mineral dust in aerosol particles, MQ water in glass vials on a shaker for 1 h, and then the WSOC concentrations were measured using a total carbon analyzer (TOC-V CSH, Shimadzu, Japan).

2.4. Estimation of available proton for mineral dust ($[H^+]_{\text{mineral}}$)

The available protons for mineral dust ($[H^+]_{\text{mineral}}$) were evaluated (see Supplemental Methods). The $[H^+]_{\text{mineral}}$ is equal to the sum of ~~estimated using the following procedures for evaluating the degree of acidification of mineral dust in aerosol~~

205 ~~particles. First, NO_3^- and $[\text{nss-SO}_4^{2-}]$ that are not~~ concentrations other than ammonium salts ($[\text{NO}_3^-]$ and $[\text{nss-SO}_4^{2-}]_{\text{non-NH}_4}$) were estimated using the following equation, assuming that $[\text{NH}_4^+]_{\text{neq}}$ was present as NH_4NO_3 and $(\text{NH}_4)_2\text{SO}_4$:

$$[\text{NO}_3^- \text{ and nss-SO}_4^{2-}]_{\text{non-NH}_4} = [\text{NO}_3^-] + 2 \times [\text{nss-SO}_4^{2-}] - [\text{NH}_4^+] \text{ (Eq. 6)}$$

Subsequently, NO_3^- and nss-SO_4^{2-} associated with ~~ammonium salt and aged~~ Na^+ in sea spray aerosols (SSA) were estimated. NaNO_3 and Na_2SO_4 are formed by chlorine depletion of SSA, as described in the following chemical reactions:



Thus, molar concentrations of $\text{NaNO}_3 + \text{Na}_2\text{SO}_4$ were equivalent to chlorine depletion from the SSA. Therefore, $[\text{NO}_3^-]_{\text{neq}}$ and $[\text{nss-SO}_4^{2-}]_{\text{neq}}$ combined with Na^+ were estimated using the following equations:

$$[\text{Cl}^- \text{ loss}] = [\text{NaNO}_3] + [\text{Na}_2\text{SO}_4] = ([\text{Cl}^-]_{\text{seawater}} / [\text{Na}^+]_{\text{seawater}}) \times [\text{Na}^+]_{\text{aerosol}} - [\text{Cl}^-]_{\text{aerosol}} \text{ (Eq. 7)}$$

215 Assuming that NO_3^- and nss-SO_4^{2-} other than ammonium and Na salts were derived from the heterogeneous reactions of HNO_3 and H_2SO_4 with mineral dust (e.g., CaCO_3), we evaluated the available acids for mineral dust ($[\text{H}^+]_{\text{mineral}}$) using the following equation:

$$[\text{H}^+]_{\text{mineral}} = [\text{NO}_3^- \text{ and nss-SO}_4^{2-}]_{\text{mineral}} = [\text{NO}_3^- \text{ and nss-SO}_4^{2-}]_{\text{non-NH}_4} - [\text{Cl}^- \text{ loss}], \text{ (Eq. 8)}$$

220 Here, $[\text{H}^+]_{\text{mineral}}$ refers to the maximum amount of strong acids (H_2SO_4 and HNO_3) that can be internally mixed with Fe-bearing particles and does not guarantee that all $[\text{H}^+]_{\text{minerals}}$ are internally mixed with the mineral particles. When $[\text{H}^+]_{\text{mineral}}$ is negative, the mineral dust in the aerosol sample was not well acidified. In contrast, if $[\text{H}^+]_{\text{mineral}}$ is higher than $[\text{nss-Ca}]$ ($[\text{H}^+]_{\text{mineral}} > 0$), mineral dust ~~may have been~~ has the potential to be acidified beyond the buffering capacity of CaCO_3 .

2.4.2.5. Iron speciation by XAFS

225 ~~Average~~The average Fe species in the aerosol samples ~~were~~was determined using bulk XAFS spectroscopy at BL-9A and BL-12C ~~in~~at the Photon Factory (PF), Ibaraki, Japan (Nomura and Koyama, 2001). ~~Synchrotron~~The synchrotron radiation generated by a bending magnet was monochromatized ~~by~~using a double-crystal monochromator of Si(111). The energy ~~resolution of the monochromator was approximately 0.2 eV.~~ Energy calibration was performed with the peak top of the pre-edge peaks of hematite aligned to 7112 eV. Approximately 1/10 of the collected aerosol samples on the PTFE filters were transferred to double-face carbon tape ~~that~~ oriented at 45° to the orthogonal direction of the incident X-ray beam. Iron K-edge XANES spectra of all the target samples were recorded ~~by~~in the fluorescence yield (FY) mode. The EXAFS spectra were simultaneously recorded with XANES for samples with sufficiently high Fe concentrations ~~high enough to obtain for~~ obtaining the EXAFS spectra. ~~Scanning~~The scanning energies of the XANES and EXAFS were 7080–7200 and 7080–7530 eV, respectively. All XANES and EXAFS spectra were recorded ~~by fluorescence yield (in the FY) mode.~~ Fluorescence X-
235 ~~ray~~rays from the samples ~~was~~were detected ~~by~~using a 19-element Ge solid-state detector equipped with a Soller slit. Spectrum analysis of the XANES and EXAFS spectra ~~were~~was performed ~~by~~using the REX2000 ~~Software~~software (Rigaku,

Japan). ~~Energy region~~The energy regions for linear combination fitting (LCF) of the XANES and EXAFS spectra ~~was~~were 7100–7200 eV and 0–10 Å in k-space, respectively.

Reference materials for inorganic Fe are ferrihydrite, goethite, hematite, weathered biotite, chlorite, illite, smectite, 240 montmorillonite, and Fe(III)-sulfate. ~~Details~~The details of these references are described ~~in~~by Takahashi et al. (2011). Iron(II)-oxalate, Fe(III)-oxalate, Fe(III)-stearate, Fe(III)-nitrate, Fe(III) complexed with deferoxamine (Fe(III)-DFO), and Fe(III)-humate were employed~~used~~ as reference materials ~~off~~for Fe(III)-organic complexes. Among ~~them~~the Fe(III)-organic complexes, Fe(III)-citrate, Fe(III)-stearate, Fe(III)-humate, and Fe(III)-DFO ~~were~~are defined generally as Fe(III)-HULIS ~~in a broad sense. The Fe(III)-HULIS can be distinguished by Fe(III)-oxalate based on Fe K-edge XANES.~~ 245 The Fe K-edge XANES and EXAFS spectra of the key species are shown in Fig. 2. ~~The XANES spectrum of Fe(III)-oxalate has two shoulders between 7120–7130 eV, whereas the sulfate showed a small shoulder in the high-energy region of the peak at 7130 eV (Fig. 2a). Iron(III)-oxalate and hematite also have an intense peak at approximately 7130 eV and a small shoulder in the low-energy region of the peak (Fig. 2a). These species were distinguished from Fe(III)-HULIS because Fe(III)-HULIS has a flat peak at 7125–7135 eV (Fig. 2a). In the case of ferrihydrite and goethite, these XANES spectra have~~ 250 a flatter peak than hematite, but the width of the peak is narrower than that of Fe(III)-HULIS ~~has flatten~~(Fig. 2a). Furthermore, the EXAFS spectrum of Fe(III)-HULIS was clearly different from that of ferrihydrite, goethite, and hematite. Fe(III)-HULIS has a single peak at 7–9 Å in the k-space, whereas Fe-(hydr)oxides have two peaks in the same region. ~~To make it easier to compare XANES spectra between reference and~~ (Fig. 2b). Based on these spectral differences, the Fe species in the aerosol samples, the XANES spectrum of the reference materials sample is shown in Fig. 6~~particles were determined using the LCF method.~~ 255 determined using the LCF method.

2.5.2.6. Al and Na speciation by XANES spectroscopy

AluminiumAl and Na speciation experiments were performed at BL-19B in PF and BL27SU in SPring-8, respectively. For both beamlines, the synchrotron radiation generated by an undulator was monochromatized ~~by~~the using a valid_ line 260 spacing plane grating monochromator (VLS-PGM). Aerosol samples on ~~the~~ carbon tape were installed in a vacuum chamber because of the short attenuation length of soft X-~~ray~~rays (< 2000 eV) in the ambient atmosphere. The Al K-edge (1550–1600 eV) and Na K-edge (1065–1100 eV) XANES spectra of the aerosol samples were recorded ~~by~~in the FY mode. Fluorescence X-~~ray~~was rays were detected ~~by~~using a single-element silicon-~~drift~~ detector.

2.6.2.7. Single-particle analysis

Single-particle analyses were conducted using ~~scanning transmission X-ray microscopy (STXM)~~ at BL-13A in PF (Takeichi et al. 2016). Monochromatic X-rays were focused ~~to~~at 30 nm × 30 nm ~~by~~using a Fresnel Zone Plate~~zone plate~~. The aerosol sample on the Mo grid was mounted on a piezo-controlled stage in a chamber purged with 0.1 atm He. Firstly, aerosol particles were imaged ~~around energies in at the~~ following energies: 280 eV (pre-edge), 285.0 eV (aromatic C), 287.6 270 eV (aliphatic C), 288.8 eV (carboxylic/hydroxamate C), carbonate (290.3 eV), and 297.2 eV (K L-edge), and 305 eV (post-

edge). ~~Iron, Na, The Fe and AlNa~~ distributions were identified by image subtraction of the post-edge from the pre-edge. The typical imaging size was $15 \times 15 \mu\text{m}^2$ with a spatial resolution of $0.06 \times 0.06 \mu\text{m}^2$. ~~After that, Subsequently, the~~ XANES spectra of C, K, Fe, Na, and Al were ~~obtained~~ separately ~~obtained by using the~~ image-stack mode. The typical ~~imaging image~~ size ~~for of~~ the image stack was $3 \times 3 \mu\text{m}^2$. ~~Image~~ ~~The image~~ drift was aligned after appending the image-stack data of all elements.

275 The XANES spectra of the regions of interest (e.g., the core and surface of the aerosol particles) were extracted using aXis2000 software.

2.7.2.8. Estimation of pH for proton-promoted dissolution (pH_{PPD})

~~Average~~ ~~The average~~ pH of the proton-promoted dissolution (pH_{PPD}) was estimated using three Fe-pool ~~model~~ ~~models~~.

280 The model was constructed based on a previous study on dissolution experiments using Beijing dust (~~dust/liquid ratio: 60 mg/L, as reported by~~ Shi et al., (2011)). ~~Three~~ ~~The three~~ Fe pools (fast, intermediate, and slow) have different dissolution rate constants according to ~~the~~ first-order kinetics (Shi et al., 2011). ~~Observed~~ ~~The observed~~ L-Fe concentration of aerosol particles ($[\text{L-Fe}(t)]_{\text{aerosol}}$) ~~was can be~~ described by the following equation:

$$[\text{L-Fe}(t)]_{\text{aerosol}} (\text{ng/m}^3 \mu\text{mol/g}) = [\text{L-Fe}(t)]_{\text{fast}} + [\text{L-Fe}(t)]_{\text{intermediate}} + [\text{L-Fe}(t)]_{\text{slow}} \quad \text{---(Eq. 69)}$$

$$[\text{L-Fe}(t)]_{\text{fast/intermediate/slow}} (\text{ng/m}^3 \mu\text{mol/g}) = [\text{obs-Fe}] \times [\% \text{Fe}(0)]_{\text{fast/intermediate/slow}} \times (1 - e^{-kt}) \quad \text{---(Eq. 710)}$$

where t is the dissolution time (h), $[\text{L-Fe}(t)]_{\text{fast/intermediate/slow}}$ is the labile Fe concentration (~~ng/m³ normalized by the mass concentration of mineral dust (μmol/g)~~) at time t , $[\text{obs-Fe}]$ is the observed total Fe concentration, $[\% \text{Fe}(0)]_{\text{fast/intermediate/slow}}$ is the percentage of solubilized Fe in each pool to the total Fe, and k is the dissolution rate constant for each pool. ~~Mass concentration of mineral dust for normalizing L-Fe concentrations was estimated by total Al concentration divided by the percentage of Al in the continental crust (8.23 %).~~ Mineral dust is expected to undergo several condensation-evaporation cycles (~~one cycle: 12 hours~~) during transport; (Pruppacher and ~~the proton~~ Jaenicke, 1995). Proton-promoted Fe dissolution ~~occurs occurred~~ during the evaporation state (wet aerosol). ~~Therefore, t is half of the transportation,~~ whereas aerosol particles were taken in cloud water during the condensation phase. According to a previous study, the global average residence times

290 ~~for aerosol particles before uptake by clouds and within the cloud in an air parcel are up to 12 h and 3 h, respectively~~ (Pruppacher and Jaenicke, 1995). Based on these residence times, aerosol particles are expected to exist in an evaporative state (wet aerosol) for approximately 67–80 % of their transport time ~~estimated by backward trajectories.~~ In this study, the estimation of pH was estimated assuming that aerosol particles spent the evaporated state in 75 % of transport time (approximately 90 h for the WPO and 130 h for CPO and SPO). The $\% \text{Fe}(0)$ and k ~~values for~~ each pool are ~~basically pH-dependent~~ described as a function of pH (Table 1). Previous studies ~~have~~ assumed illite ~~asto be~~ the major Fe species of Fe-containing ~~mineral~~ ~~minerals~~ in the slow pool. However, weathered biotite was the dominant Fe-containing mineral in our samples (see Section 3.2.) ~~Since~~. ~~Because~~ the dissolution rate of biotite is ~~about~~ ~~approximately~~ an order of magnitude higher than ~~those that~~ of illite (Bibi et al., 2011; Bray et al., 2015), the equation given in ~~the~~ ~~a~~ previous study ~~was can be~~ rewritten as follows:

300

305 Previous study: $\log k_{\text{slow}} = -0.44\text{pH} - 1.76$. (Eq. 811)

This study: $\log k'_{\text{slow}} = -0.44\text{pH} - 0.76$. (Eq. 912)

Finally, pH (optional) was given to these equations to find the pH at which the observed L-Fe could be accounted within the assumed transport time.

310 Finally, the dissolution curves at various pH values are described in Table 1. This curve with the pH of each sample was used to explain the observed L-Fe within the expected transport time. It should be noted that these kinetic parameters are estimated using the experimental data with a solid/liquid ratio of 60 mg/L. The actual aerosol dust/liquid ratios are predicted to be as high as 3000 g/L, which may suppress the dissolution of Fe from the aerosol particles (Shi et al., 2011). Our calculation results may have overestimated the modeled L-Fe concentration at pH_{PPD} with a high dust/liquid ratio. In other
315 words, a lower pH (or higher aerosol acidity) than the predicted pH_{PPD} is required to account for the observed L-Fe concentration, while considering the suppression effect. Therefore, pH_{PPD} can be recognized as the upper pH limit to explain the observed L-Fe concentration by proton-promoted dissolution.

2.8.2.9. Geochemical modelling of L-Fe species

320 Aerosol liquid water (ALW) contents were in $\text{PM}_{1.3}$, calculated by using E-AIM Model IV (Clegg et al., 1992; Friese and Ebel, 2010), which can have an agreement of ALW between observational and modeled water mass has been reported by in a previous study (Engelhart et al., 2011). The input parameters for E-AIM Model IV were the molar concentrations of H^+ , Na^+ , NH_4^+ , Cl^- , NO_3^- , and SO_4^{2-} , temperature, and relative humidity. The proton concentration was estimated using the following equation:

$$[\text{H}^+] = [\text{Cl}^-] + [\text{NO}_3^-] + 2 \times [\text{SO}_4^{2-}] - [\text{Na}^+] - [\text{NH}_4^+] \quad \text{--- (Eq. 1013)}$$

325 In this study, the buffering effect of calcite in the equilibrium calculation was not considered because (i) mineral dust was likely acidified beyond the buffering capacity of calcite, and (ii) calcite in fine aerosol particles was altered to $\text{CaSO}_4 \cdot 2\text{H}_2\text{O}$ and CaC_2O_4 during transport from the source region of Asian dust to Japan (Takahashi et al., 2008; Miyamoto et al., 2020).

The L-Fe species in aerosol liquid water (ALW) were calculated using the React model in GWB software (Bethke,
330 1996). The input data were the molar concentrations of all major ions, oxalate ions, and labile metals (Al, Mn, Fe, Ni, Cu, Zn, Cd, Ba, and Pb), WSOC, ALW, and temperature. The precipitation of metal species with a high saturation index (> 1.0) were inhibited for in the simulation of the high ionic strength conditions of ALW ($> \text{few mol/L}$, Herrmann et al., 2015). The molar concentrations of WSOC were evaluated with three types of organic species: citric acid (C6), marine aliphatic carbon (C18, Cochran et al., 2016), and deferoxamine (C25). Furthermore, L-Fe species were
335 calculated under various mixing ratios of WSOC to evaluate for evaluating the effects of the internal mixing state between L-Fe and WSOC on L-Fe species. The mixing ratio was 1.0%, 2.5%, 5.0%, 10%, 25%, 50% and 100% of WSOC concentration. For all calculations, the thermodynamic data for citric acid with Fe were used as a representative organic ligand because the stability constant and acid dissociation constant of citric acid ($\log K: -13.13$ and $\text{p}K_{\text{a}1}: -3.13$) are

similar to those of HULIS (log K_{HULIS} : 11.1–13.9 and $\text{p}K_{\text{a}}$: 3.3–4.0, Salma and Láng, 2008; Samburova et al., 2008; Abualhaija et al., 2015). The initial pH was fixed at 7 and subsequently shifted from 7 to 0 ~~to calculate for calculating~~ the pH dependence of ~~the~~ L-Fe species in ~~the~~ ALW. ~~Total~~ A total of 276 aqueous species were considered in the calculation, ~~of which and the~~ stability constants of the main species are shown in ~~the~~ Appendix ~~in of the~~ Supplemental Information.

3. Results and Discussion

3.1. Total and labile Fe and Al concentrations in TSP

Backward ~~trajectories trajectory~~ analysis was performed ~~by using~~ the ~~Hybrid Single-Particle hybrid single-particle~~ Lagrangian ~~Integrated Trajectory integrated trajectory~~ model (HYSPLIT, Stein et al., 2015). The WPO samples were affected by Asian continental outflows, whereas the air masses in ~~the~~ CPO and WPO were derived from ~~the~~ pelagic regions (Fig. ~~2S1~~). Total Fe and Al concentrations in TSP at the WPO samples (Figs. 3a and 3e, Fe: 75.6–257 ng/m³, Al: 130–422 ng/m³) were one to two orders of magnitude higher than those in the CPO and SPO (Figs. 3a and 3e, Fe: 0.733–4.37 ng/m³, Al: 3.56–4.12 ng/m³). Labile Fe and Al concentrations were also higher in ~~the~~ WPO samples (Figs. 3b and 3f, Fe: 2.61–19.8 ng/m³, Al: 3.56–27.0 ng/m³) than ~~in the~~ CPO and SPO (Figs. 3b and 3f, Fe: 0.0422–0.0489 ng/m³, Al: 0.0383–0.0678 ng/m³). Thus, ~~the~~ high total and labile metal concentrations were attributed to continental air masses (Figs. ~~23~~ and ~~3~~). ~~Enrichment factors S1~~. ~~The EF~~ of Fe in these samples were 0.26–1.8 (0.92±0.55), indicating that Fe in these TSP samples ~~were was~~ mainly derived from mineral dust (Fig. 3d). The $\text{Fe}_{\text{sol}}\%$ and $\text{Al}_{\text{sol}}\%$ in TSP were $5.30 \pm 2.99\%$ (0.967–7.69%) and $3.32 \pm 2.22\%$ (1.08–6.40%), respectively (Figs. 3c and 3g). These values were within ~~at the~~ range reported ~~by in~~ previous studies (~~Box 2 in~~ Mahowald et al., 2018 ~~and references therein~~).

3.2. Size distributions of Fe and Al concentrations

The total Fe and Al concentrations in ~~PM₄PM_{>1.3-10.2}~~ were higher than those in PM_{1.3} (Figs. 4a and 4d). ~~Iron Fe~~ and Al in ~~PM₄PM_{>1.3-10.2}~~ were accounted for $78.5 \pm 8.34\%$ (n= 5, 69.9–87.9%) and $81.8 \pm 8.53\%$ (n= 5, 72.0–88.8%) in ~~those of~~ TSP, respectively. The ~~enrichment factors EF~~ of Fe and Ti as typical crustal elements were almost 1.0, regardless of ~~aerosols aerosol~~ diameter (Fig. ~~S1S2~~). This is because mineral dust ~~is was~~ mainly present ~~in PM₄ at PM_{>1.3-10.2}~~. The labile concentrations of Fe and Al were higher in PM_{1.3} ~~than in PM₄ to PM_{>1.3-10.2}~~ (Figs. 4b and 4e). Labile Fe and Al in ~~PM₄PM_{>1.3-10.2}~~ were accounted for $60.5 \pm 34.1\%$ (n= 5, 10.7–87.3%) and $45.9 \pm 24.1\%$ (n= 5, 24.2–76.2%) in ~~those of~~ TSP, respectively. Thus, ~~the~~ size distributions of ~~the~~ L-Fe and L-Al concentrations were ~~clearly evidently~~ different from those of ~~the~~ total Fe and Al. The average $\text{Fe}_{\text{sol}}\%$ in ~~PM₄PM_{>1.3-10.2}~~ and PM_{1.3} were $2.56 \pm 2.53\%$ (n=20, 0.00–8.50%) and $22.3 \pm 21.7\%$ (n=10, 0.202–64.7%), respectively (Fig. 4c). In the case of Al, the average $\text{Al}_{\text{sol}}\%$ in ~~PM₄PM_{>1.3-10.2}~~ and PM_{1.3} were $2.76 \pm 2.85\%$ (n=20, 0.389–11.5%) and $11.7 \pm 10.8\%$ (n=10, 0.700–32.4%), respectively (Fig. ~~4e4f~~). Thus, both Fe and Al in ~~PM₄PM_{>1.3}~~ were more soluble than those in ~~PM₄PM_{>1.3-10.2}~~. Therefore, even if the total Fe concentration in PM_{1.3} was lower than ~~PM₄ that in PM_{>1.3-10.2}~~, ~~the~~ PM_{1.3} plays a significant role in supplying Fe ~~into~~ the ocean surface.

The ~~enrichments~~enrichment of labile Fe and Al in ~~fine fractions~~PM_{1.3} has been reported ~~by~~in previous studies (Baker and Jickells, 2006; Buck et al., 2010; Chance et al., 2015; Baker et al., 2020; Kurisu et al., 2021). One of the reasons for the enrichment of labile Fe in ~~fine fractions~~PM_{1.3} is the presence of ~~pyrogenic~~anthropogenic Fe in ~~fine fractions~~PM_{1.3} (Kurisu et al., ~~2021~~2016; 2021; Hsieh et al., 2022). It is known that anthropogenic Fe is emitted as Fe oxides with a small amount of coexisting elements, which should affect the EF of Fe. In fact, the EF of Fe in PM_{1.3} impacted by anthropogenic Fe, was higher than 2.0 (Kurisu et al., 2016, 2019; Hsieh et al., 2022; Zhang et al., 2022). However, the EF of Fe in our samples was almost 1.0 (Fig. S2), indicating that the influence of anthropogenic Fe oxides was insignificant. Oil ~~combustions~~combustion, including ship emissions, ~~are~~is one of the dominant sources of pyrogenic Fe in ~~fine aerosol particles~~because ~~PM_{1.3} as~~ several studies have ~~been~~reported ~~associations of~~good correlations between high Fe_{sol}% ~~with~~and high ~~EFs~~EFs of V and Ni (Sedwick et al., 2007; Sholkovitz et al., 2009; Ito, 2015). However, Fe_{sol}% in PM_{1.3} ~~were~~was not correlated with ~~the~~ EF of V and Ni (Table S3, Spearman's correlation factor rho (ρ): ~~0.36~~as tracers of oil combustion (Figs. 5a and ~~-0.25 for V and Ni, respectively~~5b), which ~~was~~is consistent with ~~a previous~~the results of an observational study of the Pacific Ocean (Buck et al., 2013). ~~In contrast,~~

Coal fly ash is a dominant source of Fe in marine aerosol particles (Schroth et al., 2009; Sedwick et al., 2007; Sholkovitz et al., 2009; Chen et al., 2012; Ito, 2015; Baldo et al., 2022). Fe_{sol}% in PM_{1.3} ~~were~~correlated with ~~the~~ EF of Pb (Table S3, ρ: ~~0.75 for Pb~~and nss-SO₄²⁻ (Figs. 5c and 5d), which ~~were useful tracers~~is a good tracer for municipal solid waste incineration (~~MSWI~~) and coal ~~combustions~~combustion in terrestrial regions (Nriagu and Pacyna, 1988; Sakata et al., 2000, 2014). ~~However, L-Fe in our samples were unlikely~~Since the EF of Fe in coal fly ash is close to 1, ~~distinguishing between mineral dust and coal fly ash based on the EF of Fe is difficult~~ (EF was calculated using NIST reference materials, Table S2). ~~In contrast, coal and coal fly ash tended to be enriched in Co (EF~10, Table S2). Assuming that the Fe_{sol}% (mean: 22.4%) in PM_{1.3} can be associated with high soluble Fe in coal fly ash (Fe_{sol}%, 100%) with high EF of Co (~10), the EF of Co in the PM_{1.3} becomes approximately 3.0. Because the actual Fe_{sol}% of coal fly ash is lower than 100% (Chen and Grassian, 2013; Baldo et al., 2022), it is expected that EF of Co in PM_{1.3} is more than 3.0. However, the EFs of Co in the PM_{1.3} samples were approximately 1 (Fig. S2), indicating that coal fly ash was not the dominant source of L-Fe in the samples. Moreover, the correlation between Fe_{sol}% and the EF of Pb was spurious. The spurious correlation was caused by nss-SO₄²⁻ as the conjunction factor due to the good correlations of nss-SO₄²⁻ with Fe_{sol}% and EF of Pb (Figs. 5d and 5e). The residuals of Fe_{sol}% and EF of Pb from their regression lines versus nss-SO₄²⁻ were determined to evaluate the direct relationship between Fe_{sol}% and EF of Pb, excluding the influence of nss-SO₄²⁻ for both factors. As a result, the residue of Fe_{sol}% did not correlate with the EF of Pb (Fig. 5f, partial correlation coefficient: -0.15), indicating that the direct emission of L-Fe from coal combustion was not a significant source.~~

The concentration of [H⁺]_{mineral} is higher than [nss-Ca²⁺] in PM_{1.3} with high Fe_{sol}% (>10 %). This result implies that mineral dust was acidified beyond the buffering capacity of calcite (Figs. 6a–6c). The dominant source of [H⁺]_{mineral} in the WPO samples was mainly SO₂ or H₂SO₄ because the NO₃⁻ concentrations were lower than those of nss-SO₄²⁻ (Fig. S3a and 3b). The sources of nss-SO₄²⁻ in East Asia and its outflow were mainly derived from anthropogenic ~~sources~~because ~~EFs of~~

410 Fe in $PM_{1.3}$ were almost 1.0 above mentioned (Fig. S1). The $PM_{1.3}$ with high $Fe_{sol}\%$ ($>10\%$) contained available proton for mineral dust ($[H^+]_{mineral}$; see the Method section), whereas those in $PM_{1.3-10.3}$ and $PM_{1.3}$ with low $Fe_{sol}\%$ ($<10\%$) were near 0 or negative (Fig. 5a). Furthermore, the $[H^+]_{mineral}$ in $PM_{1.3}$ with high $Fe_{sol}\%$ was higher than $[nss-Ca^{2+}]$, indicating that $[H^+]_{mineral}$ acidified mineral dust beyond the buffer capacity of $CaCO_3$ (Figs. 5b and 5c). In fact, $Fe_{sol}\%$ in $PM_{1.3}$ were also correlated with $nss-SO_4^{2-}$ (Table S3, $\rho: 0.81$), but a good correlation between $Fe_{sol}\%$ and oxalate was not observed (Table S3, $\rho: 0.20$). Therefore, it seems that aerosol acidification is more significant compared to organic complexations and anthropogenic emissions to solubilize Fe in $PM_{1.3}$.

415 In the case of WPO samples, it is considered that mineral dust was acidified during transportation in East Asia because East Asia is a highly polluted area in the world owing to the lower S isotope ratio (about few ‰, Inomata et al., 2016; Chung et al., 2019) than that of biogenic S (18-20 ‰, Amrani et al., 2013). Previous studies showed that mineral dust in East have reported that the good relationship between $Fe_{sol}\%$ and $nss-SO_4^{2-}$ is attributed to the solubilization of Fe by coal-derived SO_2 (Fang et al., 2015; Wong et al., 2020), and a good correlation between $Fe_{sol}\%$ and $nss-SO_4^{2-}$ was found in this study (Fig. 5d). This result is consistent with previous studies because Asian aerosol contained dust, especially aluminosilicate, in $PM_{1.3}$ is internally mixed with sulfate and oxalate as a proof of particle acidifications (Sullivan et al., 2007; Fitzgerald et al., 2015; Li et al., 2017; Sakata et al., 2021). Therefore, the acidification of mineral dust during transport in East Asia is the dominant reason for the high $Fe_{sol}\%$ in $PM_{1.3}$ collected in the WPO. Although $PM_{1.3}$ in the CPO sample did not pass over the highly polluted region, the S6-CPO has had a positive $[H^+]_{mineral}$ and high $Fe_{sol}\%$. This result is probably due to the acidifications of mineral dust by SO_2 and H_2SO_4 derived from biogenic S (e.g., dimethylsulfide) because NH_3 gas cannot fully neutralized biogenic SO_2 and H_2SO_4 (Paulot et al., 2015; Nault et al., 2021). In fact, the $nss-SO_4^{2-}$ concentration in S6-CPO was approximately an order of magnitude higher than that of NH_4^+ (Figs. S3b and S3c); similar results have been reported in previous studies (Paulot et al., 2015; Nault et al., 2021). S2a and S2b). Thus, $Fe_{sol}\%$ in $PM_{1.3}$ was enhanced by aerosol acidifications in not only polluted regions but also marine atmosphere. The possible sources of SO_2 and H_2SO_4 in the Pacific Ocean in the Southern Hemisphere are mainly biogenic S (e.g., dimethyl sulfide), which is indicated by the S isotope ratio (Calhoun et al., 1991; Li et al., 2018). Moreover, it is known that mineral dust is internally mixed with sulfate through cloud processes, even if it does not pass over the polluted region (Fitzgerald et al., 2015). Therefore, the mineral dust in the CPO samples was likely acidified by biogenic S during transport.

3.3. Size dependence of Fe species in marine aerosols

435 Iron species in PM_4 and $PM_{>1.3-10.2}$ were composed of two or three Fe species of hematite, ferrihydrite, biotite, and illite (Figs. 6a, 6e, 7a, 7b, and S3S4). More than half of the Fe in $PM_{1.3-10.2}$ was composed of biotite (Fig. 6a, 7a). The EXAFS spectra of PM_4 and $PM_{>1.3-10.2}$ well accurately reflected the spectrum feature of biotite in 7–9 Å of k-space (Fig. S4, Figs. S5a–S5c), indicating that biotite was the dominant Fe species in PM_4 and $PM_{>1.3-10.2}$. The relative abundance of ferrihydrite increased with decreasing aerosol diameter and with increasing transportation distance (Fig. 6a, 7a, transport distance: WPO1 <

WPO2 < WPO3 < SPO \cong CPO). The hydration reaction of phyllosilicates in ~~PM_{1.3}+PM_{>1.3+0.2}~~ forms secondary ferrihydrite during ~~transportation~~ (Takahashi et al., 2011). Therefore, Fe in biotite ~~in the PM_{1.3} at PM_{>1.3+0.2}~~ was partially altered to ferrihydrite. The Fe species in PM_{1.3} with negative [H⁺]_{mineral} (S5-WPO1 and S6-SPO₂), were composed of the same species in ~~PM_{1.3}+PM_{>1.3+0.2}~~ (Figs. 6a and 7a). The negative [H⁺]_{mineral} ~~means value indicates~~ that the mineral dust was not acidified beyond the buffering ~~capacities~~ capacity of CaCO₃. Therefore, the Fe species in ~~PM_{1.3}+PM_{>1.3+0.2}~~ and PM_{1.3} were not drastically modified by aerosol acidification.

445 Iron(III)-HULIS and Fe(III)-sulfate were found as characteristic Fe species in PM_{1.3} with [H⁺]_{mineral} and high Fe_{sol}% (>10 %, Figs. 6a, 6e7a, 7b, and S3S4). Iron(III)-HULIS was present in all PM_{1.3} with positive [H⁺]_{mineral}, whereas only S6-WPO3 contained Fe(III)-sulfate ~~with and~~ Fe(III)-HULIS (Fig. 6a7a). Since the source of Fe in PM_{1.3} was mineral dust (~~Fig. S1~~), the Fe species at the time of emission was thought to be similar to that of ~~coarse particles. However, the EXAFS spectra of PM_{1.3}+PM_{>1.3}. However, the EXAFS spectra of PM_{1.3}~~ reflected spectrum features of Fe(III)-HULIS and Fe(III)-sulfate rather than biotite (Fig. S4S5). It ~~seems appears~~ that Fe(III)-sulfate and Fe(III)-HULIS were formed by secondary processes of biotite during transport. ~~It Oxalate is known that oxalate is one of the an~~ important ~~ligands to enhance ligand for enhancing~~ Fe_{sol}% in aerosol particles (Chen and Grassian, 2013; Ito and Shi, 2016; Hamilton et al., 2019), ~~and~~ the presence or ~~the~~ absence of Fe(III)-oxalate in these samples ~~were was~~ examined. As a result, the abundance of ~~the Fe(III)-oxalate~~ in these samples was not ~~the~~ dominant Fe species in our samples ~~obtained~~ by ~~the~~-LCF. This result is consistent with the fact that

455 there ~~is was~~ no ~~correlations~~ correlation between ~~the~~ Fe_{sol}% and oxalate concentrations (~~Table S3~~ Spearman's $\rho = 0.20$).

For comparison, ~~the~~ Fe species in East Asian aerosols (Beijing and NOTOGRO) were determined by XAFS spectroscopy. ~~The EF of Fe and Fe_{sol}% in Beijing dust were 0.85 and 0.53 % (MQ extraction at 100 g/L of the dust/liquid ratio), respectively. Although the sampling year of the sample collected in NOTOGRO was different from that of the marine aerosol particles, the backward trajectory, EF of Fe, and Fe_{sol}% in the sample collected in the sample were similar to those of~~

460 ~~the marine aerosol particles (Fig. S6a–S6d). Therefore, this sample was used as a proxy for the chemical alteration of Fe in size-fractionated aerosol particles during transport from East Asia to Japan.~~ Beijing dust also contained Fe(II)-sulfate and Fe(III)-sulfate with ferrihydrite and biotite (~~Fig. S5~~). ~~Iron. Relative abundances of these species in PM_{1.3} to total Fe were 9 %, 11 %, 44 %, and 36 %, respectively (Fig. S4d). The iron species in PM_{>1.3+0.2} collected in the NOTGRO, were composed of illite, smectite, biotite, and ferrihydrite, the species of which species were similar to those in PM_{1.3}+PM_{>1.3+0.2} in marine aerosol particles (Figs. 6a7a and 6e7c), whereas Fe(II)-sulfate and Fe(III)-oxalate ~~was were~~ found in PM_{1.3} collected in ~~the~~ NOTOGRO (Figs. 6a7a and 6e7c). The EXAFS spectrum of ~~the~~-S6-NT has a single peak in 7–9 Å of k-space, whereas those of ~~PM_{1.3}+PM_{>1.3+0.2}~~ has two peaks of biotite in the same regions (Fig. S4eS5d). Therefore, Fe(II)-sulfate and Fe(III)-oxalate were formed by ~~the~~ chemical alteration of biotite, which ~~was is~~ consistent with ~~the~~ Fe speciation results of WPO. Iron(III)-HULIS was not ~~assigned identified~~ as the dominant Fe species in NOTOGRO and Beijing dust (Figs. 6a, 6e5a and S5S5d).~~

470 These results ~~indicated indicate~~ that Fe(III)-HULIS in the WPO samples was possibly formed by ~~the~~ chemical alteration of Fe(II, III)-sulfates and Fe(III)-oxalate after aerosol ~~pass passes~~ over Japan.

To identify ~~the~~ L-Fe species in PM_{1.3}, Fe K-edge XANES spectra of insoluble Fe in ~~the~~ S6-WPO2 were recorded after ~~the~~ water ~~extraction~~ extraction of labile Fe species. ~~As a result, the~~ ~~The~~ XANES spectra of total Fe (~~=~~(labile + insoluble Fe) ~~was~~ ~~were~~ well fitted by insoluble Fe and Fe(III)-HULIS (Fig. ~~S3d~~~~S4e~~). Furthermore, the Fe_{sol}% in PM_{1.3} ~~were~~ ~~was~~ correlated with the abundance of Fe(III)-HULIS (Fig. ~~6e~~~~7d~~). Therefore, Fe(III)-HULIS is an important L-Fe species in PM_{1.3} in the marine atmosphere.

3.4. Size dependence of Al species

Given that Fe(III)-HULIS was formed by chemical alterations of Fe in biotite, ~~the~~ Al species in PM_{1.3} may be different from those in ~~PM₄PM_{>1.3+0.2}~~. Therefore, we determined ~~the~~ Al species in WPO2 and WPO3 ~~using~~ ~~by~~ XANES spectroscopy. The Al species in ~~PM₄PM_{>1.3+0.2}~~ were composed of octahedral Al and tetrahedral Al, of which ~~the~~ Al K-edge XANES spectra were similar to those of biotite (Fig. ~~7~~ ~~8~~). ~~Moreover, the~~ Al K-edge XANES spectra of ~~PM₄PM_{>1.3+0.2}~~ were well fitted by each other. This result implies that (i) the ~~sources of dominant~~ Al ~~emissions~~ ~~species in~~ PM_{>1.3} were ~~similar among PM_{4,3+0.2}:1 phyllosilicate, including biotite~~, and (ii) Al species in these samples ~~were~~ ~~did~~ not ~~changed~~ ~~change~~ significantly during transport. In contrast, secondary Al species were identified in ~~the~~ PM_{1.3}. ~~The Gibbsite was found in S5-WPO2 and S5-WPO3 contained gibbsite and phyllosilicates (Fig. 7), with which abundances of 20 % and 30 % in total Al, respectively (Figs. 8a and 8b).~~ The S6-WPO3 contained Al-sulfate and organic complexes of Al (organo-Al) ~~in addition to phyllosilicates in PM_{4,3+0.2} and gibbsite, which was~~, gibbsite, and phyllosilicates, and their abundances were 8 %, 8 %, 18 %, and 66 %, respectively. ~~The presence of organo-Al and Al-sulfate in S6-WPO3 is consistent with the presence that~~ of Fe(III)-sulfate in this sample (Figs. ~~6a~~ ~~7a~~ and ~~88b~~). In the case of S6-WPO2 ~~with the highest abundance of Fe(III)-HULIS~~, the Al K-edge XANES spectrum was ~~totally~~ ~~completely~~ different from that of phyllosilicates ~~in PM_{4,3+0.2}, though at PM_{>1.3} (Fig. 8a), although~~ the XANES spectrum of S6-WPO2 could not be fitted by the reference materials examined in this study. Given that ~~the~~ initial Al species in PM_{1.3} were ~~phyllosilicate~~ ~~phyllosilicates~~, as was ~~the case~~ for ~~PM₄PM_{>1.3+0.2}~~, it is possible that phyllosilicate particles were altered in the atmosphere. This result is consistent with the absence of the ~~spectrums~~ ~~spectral~~ feature of biotite in ~~the~~ Fe K-edge EXAFS spectra of PM_{1.3}.

3.5. Single-particle analysis

Single-particle analysis ~~in~~ ~~of~~ S6-WPO2 was conducted using STXM ~~to evaluate~~ ~~for evaluating~~ the alteration processes of Fe-bearing phyllosilicate particles. Iron-bearing particles ~~have~~ ~~had~~ irregular shapes (Figs. ~~8S7~~ and ~~S6~~ ~~S8~~). This morphological feature ~~was~~ ~~is~~ similar to ~~that of~~ naturally occurring phyllosilicate particles (Matsuki et al., 2005; Jeong and Nousiainen, 2014). In contrast, anthropogenic Fe (e.g., fly ash and pyrogenic hematite) has spherical shapes ~~which were~~ ~~that are~~ not ~~dominated~~ ~~dominant~~ in S6-WPO2 (Li and Shao, 2009; Adachi et al., 2021). Therefore, Fe-bearing particles with irregular shapes ~~and high~~ ~~OD_{C-pre}~~ were phyllosilicate particles. These Fe-bearing phyllosilicates ~~were~~ ~~are~~ covered with Na and OCs. ~~Organic carbons on mineral dust were mainly presented as aliphatic species because the peaks of aliphatic C and carboxylates were dominated in the~~ ~~The carbon~~ K-edge NEXAFS spectra (Fig. ~~8~~ and ~~S8~~). ~~The C K-edge NEXAFS spectra~~

of OCs on the mineral on the surface of mineral dust were similar to those of OCs in submicron sea spray aerosol SSA particles reported in previous studies (Prather et al., 2013; Wilson et al., 2015). Furthermore, the Na K-edge XANES spectra species on the particle surface were also similar to the Na salt with organic acids rather than inorganic Na (Fig. S9). It is known that submicron sea spray aerosol (SSA) (Figs. S8 and S9d), for which the Na K-edge XANES spectra were similar to the average Na species in PM_{1.3} collected in WPO2 and WPO3 (Figs. S9a and S9b). Submicron SSA and marine cloud water contained both Na and OCs (Mochida et al., 2002; Straub et al., 2007; Cochran et al., 2016; Bikina et al., 2019). In fact, the Na speciation result also showed that PM_{1.3} collected in WPO2 and WPO3 contained organic Na salts, whereas Na species in PM_{1.3-10.2} was composed of only NaCl (Fig. S9). Therefore, submicron SSA or marine cloud water is one of the sources of Na and OCs on the phyllosilicate surface. The surface coating of Na and OCs contributed to chemical alteration of phyllosilicate particles because Al K-edge XANES spectra of these particles were similar to that in humic substances (SRFA, Fig. 7). Thus, phyllosilicate particles in PM_{1.3} were intensely altered during transport from East Asia to the WPO (2019). Therefore, it is considered that the mineral dust gained Na and OCs on the particle surface through cloud processes.

Similar internal mixing particles between mineral dust and SSA have been found not only in the Pacific Ocean, but also in other regions (Okada et al., 1990; Niimura et al., 1998; Wagner et al., 2008; Kandler et al., 2017; Adachi et al., 2020; Kwak et al., 2022; Knopf et al., 2022). It is considered that the internal mixing of mineral dust and sea salt is formed by cloud processes (Niimura et al., 1998; Formenti et al., 2011). A recent study found internal mixing particles between aged sea salt, mineral dust, S, and OCs in submicron aerosols collected from the North Atlantic Ocean, of which OCs species were similar to those in SSA (Knopf et al., 2022). This result is similar to the microscopic observation results (Figs. S7 and S8). Since (i) SSA is ubiquitously present in the marine atmosphere and (ii) the chemical composition of marine cloud water is influenced by SSA, the internal mixing of mineral dust with SSA in cloud water may play a significant role in the organic complexation of L-Fe in aerosol particles in the marine atmosphere.

4. Discussion

4.1. Reconstruction alteration processes of Fe based on pH_{PPD} and pH_{L-Fe}

Our observation results showed that L-Fe in aerosol particles were mainly controlled by Fe in PM_{1.3} (Fig. 4b4c). Aerosol acidification was one of the factors of enhancement of L-Fe concentrations because (i) PM_{1.3} with high Fe_{sol}% (>10%), has positive $[H^+]_{\text{mineral}}$ (Fig. 5a6a), and (ii) L-Fe concentration correlated with $[nss-SO_4^{2-}]$ (Table S3 Fig. 5d). Furthermore, Fe(III)-HULIS was found in PM_{1.3} with a positive $[H^+]_{\text{mineral}}$, of which the fraction of Fe(III)-HULIS correlated with Fe_{sol}% in aerosol particles (Fig. 6e7d). Therefore, it is likely that both aerosol acidification and organic complexation of Fe contributed to the enhancement of Fe_{sol}%. Here, The reaction pH for proton-promoted dissolution (pH_{PPD}) and formation of L-Fe species (pH_{L-Fe}) were evaluated using conceptual and geochemical models, respectively. Firstly, the modelled L-Fe concentration in PM_{1.3} with a negative $[H^+]_{\text{mineral}}$ was much higher than the observed L-Fe concentration, even though pH_{PPD} was set as 3.0 (Fig. S10). This result indicates that the Fe-bearing particles in

540 these samples were not acidified to a pH of 3.0. Consequently, Fe in these samples was not sufficiently solubilized by atmospheric processes. In fact, the Fe species in these samples were similar to those in $PM_{1.3+0.2}$ with low $Fe_{sol}\%$.

The observed L-Fe concentrations in $PM_{1.3}$ with positive $[H^+]_{\text{mineral}}$ were reproduced when the pH was lower than ≤ 3.0 (Figs. 9a, 9c, and S11). This result is consistent with those of previous studies because the high $Fe_{sol}\%$ was observed when the aerosol pH was lower than 3.0 (Fang et al., 2017; Tao and Murphy, 2019). As previously mentioned, the Fe in the biotite was altered to Fe(III)-HULIS and/or Fe(III)-sulfate (Fig. S4). Previous studies showed have shown that the octahedral layer of phyllosilicate phyllosilicates, including biotite were, is preferentially decomposed under highly acidic conditions ($pH < 3.0$) and Fe in biotite is mainly present in the octahedral layer (Shaw et al., 2009; Bray et al., 2015). Therefore, it is reasonable that $Fe_{sol}\%$ increases increased rapidly when the pH drops dropped below 3.0. Modelled The modeled L-Fe species in $PM_{1.3}$ with positive $[H^+]_{\text{mineral}}$ were present as Fe(III)-sulfate or Fe(III)-oxalate under acidic conditions ($pH_{L-Fe} < 3.0$) with any ratios ratio of [citrate]/[oxalate] and [citrate]/[L-Fe], though although the stability constants of citrate is are much higher than that those of oxalate and sulfate (Fig. 9 Figs. 9b, 9d, and S12–16). This phenomenon can be ascribed to the fact that citric acid forms fully protonated species below its pK_{a1} ($= 3.13$), whereas oxalate and sulfate can form ferric complexes, even at $pH < 3.0$ (Fig. 9 Figs. 9b, 9d, and S12–16). As previously mentioned, the East Asian aerosol particles contained Fe(II, III)-sulfate and Fe(III)-oxalate, but Fe(III)-HULIS was not the dominant Fe species (Figs. 6a, 6d and S5S4d). Therefore, it is considered that the mineral dust in the WPO samples encountered the highly acidic conditions during transportation in East Asia. By contrast, the CPO sample did not pass over the polluted region (Fig. S1b), and positive $[H^+]_{\text{mineral}}$ and low pH_{PPD} were observed in S6-CPO (Figs. 6a and S11a). Aluminosilicate particles react with sulfate through cloud processes, even if the particles do not pass over the polluted region (Fitzgerald et al., 2015). Moreover, a previous study reported that the $Fe_{sol}\%$ in Saharan dust was increased by aerosol acidification by $nss-SO_4^{2-}$ during long-range transport in the Atlantic Ocean (Longo et al., 2016). Therefore, similar reaction processes can promote the acidification of the CPO sample. Although $nss-SO_4^{2-}$ in the pelagic region is thought to be derived from biogenic origins (Calhoun et al., 1991; Li et al., 2018), further studies are required for determining the effect of biogenic S on the increase in $Fe_{sol}\%$.

In contrast, the geochemical model showed that Fe(III)-HULIS was dominant under moderately acidic conditions (pH_{L-Fe} 3.0–6.0), where the [citrate]/[L-Fe] ratio was higher than 1.0 (Figs. 9b, 9d, and S12–S16). In the case of S6-WPO3, the coexistence of Fe(III)-HULIS and Fe(III)-sulfate was found only under only moderately acidic conditions, when [citrate]/[L-Fe] was between 0.30 and 0.45 (Figs. 9d and S16). Therefore, the pH of phyllosilicate phyllosilicates should be increased after proton-promoted processes to form the Fe(III)-HULIS. Single-particle analyses identified the presence of a surface coating of Na and OCs on phyllosilicate particles, which was caused by internal mixing with submicron SSA or marine cloud water (Fig. S7 and S8). A recent mesocosm experiment showed that submicron SSA is rapidly acidified to pH 2.0 because of water evaporation, uptake of acidic gases, and/or displacement reaction of proton protons in organic acids by Na^+ (Angle et al., 2021). Our Na speciation results showed that the organic salt of Na was present in the submicron SSA (Fig. S8S9). If submicron SSA in the ambient atmosphere has high aerosol acidity, the internal mixing of phyllosilicates and submicron SSA may not sufficiently increase the pH of phyllosilicates.

Another ~~candidate~~potential process for increasing aerosol pH is the evaporation–condensation ~~eye~~cycle (cloud
575 process) during transportation. ~~The marine~~Marine cloud water can also ~~can~~ form Na and OCs ~~coating~~coatings on the
phyllosilicate particles because Na and OCs ~~are~~are dominant components in ~~the~~ marine cloud water (Straub et al., 2007).
Given that 500 nm of phyllosilicate particles with a 100 nm-thick water layer at pH 1.0 was incorporated into typical marine
cloud water (diameter 10 μm , pH 4.0, Boris et al., 2016; Kim et al., 2019; Shah et al., 2020), the pH of ~~the cloud water~~
~~decreased by only 0.03 pH unit~~aerosol particles was 3.97. The increase in aerosol pH by cloud processes decreases $\text{Fe}_{\text{sol}}\%$
580 because of the precipitation of nano-ferrihydrate, with the sole consideration of inorganic Fe chemistry (Spokes et al., 1994;
Shi et al., 2015; Maters et al., 2016). However, ~~the nano-ferrihydrate~~ ~~precipitations were~~precipitation was suppressed by the
formation of Fe(III)-HULIS ~~due~~owing to its high solubility. As a result, L-Fe obtained by proton-promoted dissolution
below pH 2.0 was retained under moderately acidic conditions. Therefore, the role of HULIS is not to ~~promote~~encourage
further Fe dissolution from aerosol particles, but to stabilize ~~the L-Fe~~ ~~under~~under moderately acidic conditions. This result
585 was consistent with that of a previous laboratory experiment (Paris and Desboeufs, 2013).

In summary, Fe in $\text{PM}_{1.3}$ was solubilized by ~~the~~ proton-promoted dissolution, and subsequently, solubilized Fe ~~were~~was
stabilized as L-Fe by organic complexation with HULIS in the cloud processes (Fig. 10). In the case of the WPO samples,
aerosol acidification and stabilization of L-Fe ~~was caused~~occurred in East Asia and the Pacific Ocean, respectively. This
result is consistent with the hypothesis ~~suggested~~proposed by Buck et al. (2013). ~~The~~These studies ~~implied~~imply
590 atmospheric processing after passing over Japan ~~are~~is not important ~~to solubilize~~for solubilizing Fe because significant
differences ~~of~~in $\text{Fe}_{\text{sol}}\%$ in the North Pacific Ocean ~~has~~have not been observed (Buck et al., 2013). The stabilization of L-Fe
species may play a critical role in the supply of dissolved Fe from aerosol particles to the ocean surface. Given that log
 K_{HULIS} in aerosol particles is a strong ligand on the ocean surface (L_1 , log $K > 12$), Fe(III)-HULIS ~~dissolved~~dissolves without
the consumption of L_1 ligands on the ocean surface. This phenomenon possibly promoted further Fe dissolution with
595 moderately water-soluble species (e.g., nano-ferrihydrate) by complexation with ~~the~~ L_1 or weaker ligands (L_2 , log $K: -11$ – -12)
on the ocean ~~surfaces~~surface (Gledhill and Buck, 2012). When log K_{HULIS} was similar to weak or super-weak ligands (log K
< 11), the ~~probabilities~~probability of encountering L_1 and L_2 ligands with Fe(III)-HULIS increased by with
lifetime of dissolved Fe (hours to days, Meskhidze et al., 2017). Thus, Fe(III)-HULIS strongly influences the fate of
dissolved Fe in the ocean from the aerosol particles. Further ~~investigations~~investigation of atmospheric organic ligands
600 combined with Fe in aerosol particles ~~are~~is necessary ~~to extend our~~ for gaining further knowledge ~~of~~of the biogeochemical
cycle of Fe.

4.2. Importance of size-fractionated aerosol particles

Thus, the Fe in $\text{PM}_{1.3}$ was solubilized by atmospheric processes during transportation. These results could not be
605 obtained if we collected ~~TSP~~, rather than size-fractionated aerosol particles. This is because the abundance of Fe(III)-HULIS

is approximately 5% of total Fe in TSP, which ~~wasis~~ below the detection limit of XAFS spectroscopy. Previous studies have also suggested the presence of Fe(III)-sulfate as ~~an~~ L-Fe species by spot analysis using microscopic XAFS, but Fe(III)-sulfate ~~were~~ was not detected by macroscopic XAFS because of ~~the~~ lower abundance of the species in TSP (Oakes et al., 2012; Kurisu et al., 2021). Therefore, size-fractionated aerosol sampling is ~~needed~~ required to identify ~~the~~ L-Fe species in ~~the~~ marine aerosol particles.

In general, the ~~cut-off~~ diameter for size-fractionated aerosol sampling is 2.5 μm , but this may not be ~~enough~~ sufficient to separate the L-Fe species with high $\text{Fe}_{\text{sol}}\%$ from the less aged mineral dust. Our results showed that ~~a~~ high $\text{Fe}_{\text{sol}}\%$ associated with Fe(III)-HULIS was found in $\text{PM}_{1.3}$. In contrast, aerosol particles in stage-4 (~~hereafter, $\text{PM}_{1.3-2.3}$ is described as $\text{PM}_{1.0-2.5}$ for the simplification~~) did not have ~~a~~ high $\text{Fe}_{\text{sol}}\%$ because mineral dust in the ~~fractions~~ fraction was not acidified ~~beyond the buffering capacity because of CaCO_3 ; the negative $[\text{H}^+]_{\text{mineral}}$~~ . This result is consistent with previous studies because ~~the~~ aerosol pH in $\text{PM}_{1.0-2.5}$ was higher than ~~those that~~ in $\text{PM}_{1.0}$ ~~because of, owing to the~~ larger and smaller contributions of non-volatile cations (e.g., Ca and Na) and sulfates in $\text{PM}_{1.0-2.5}$ compared to $\text{PM}_{1.0}$, respectively (Fang et al., 2017; Guo et al., 2018). Furthermore, in ~~the case of~~ our sample, ~~about~~ approximately 40% (11.9–58.9%) of the total Fe in $\text{PM}_{2.5}$ was contained in $\text{PM}_{1.0-2.5}$. In the analysis of ~~the~~ $\text{PM}_{2.5}$, the relative abundances of L-Fe concentrations in $\text{PM}_{1.0}$ were diluted by insoluble Fe in $\text{PM}_{1.0-2.5}$. This is also ~~true for~~ relevant to the investigation of pyrogenic Fe with high $\text{Fe}_{\text{sol}}\%$. Previous studies ~~showed~~ have shown that ~~a~~ low Fe isotope ratio associated with pyrogenic Fe ~~wasis~~ found in $\text{PM}_{1.3}$, whereas the isotope ratio in $\text{PM}_{1.0-2.5}$ ~~wasis~~ similar to ~~that of~~ Fe in crustal materials (Kurisu et al., 2016, 2019). For these reasons, two-stage aerosol sampling with a ~~cut-off~~ diameter of 1.0 μm or multi-stage aerosol sampling is desirable ~~to~~ ~~investigate for~~ investigating the factors controlling ~~the~~ $\text{Fe}_{\text{sol}}\%$ in marine aerosol particles. ~~Since~~ Because size-fractionated aerosol sampling ~~recovered~~ recovers a small amount of sample ~~er each stage~~ per stage compared to TSP sampling (Sakata et al., 2018; Baker et al., 2020), the ~~developments~~ development of analytical techniques for low ~~concentration~~ concentrations of trace ~~metal are~~ metals is essential.

5. Conclusions

In this study, size-fractionated aerosol particles were collected in the Pacific Ocean. About 80% of total Fe were present in ~~PM_1~~ $\text{PM}_{>1.3-10.2}$, whereas $\text{PM}_{1.3}$ accounted for about 60% of L-Fe in TSP. The average $\text{Fe}_{\text{sol}}\%$ in $\text{PM}_{1.3}$ (22.3 \pm 21.7%) was about an order magnitude of higher than that in ~~PM_1~~ $\text{PM}_{>1.3-10.2}$ (2.56 \pm 2.53%). The Fe species in ~~PM_1~~ $\text{PM}_{>1.3-10.2}$ were ferrihydrite, hematite, biotite, and illite. These Fe were similar to those in mineral dust. The Fe in ~~PM_1~~ $\text{PM}_{>1.3-10.2}$ was not well solubilized during transportation because mineral dust in the fraction was not acidified beyond the buffering capacity of CaCO_3 . ~~In~~ In the case of $\text{PM}_{1.3}$ with positive $[\text{H}^+]_{\text{minerals}}$, Fe(III)-HULIS was present as specific L-Fe species in $\text{PM}_{1.3}$. The species were formed by the chemical alteration of biotite. The chemical alteration of biotite in $\text{PM}_{1.3}$ was confirmed by bulk Al speciation and single-particle analysis of mineral dust because secondary Al species (e.g., gibbsite,

Al-sulfate, and organo-Al) were present in the PM_{1.3}. Thus, the Al species can be used as a good indicator of the degree of phyllosilicate alterations. As a result of pH estimation using a conceptual model, Fe in mineral dust was solubilized under highly acidic conditions ($pH_{HPPD} < 3.0$). Subsequently, Fe(III)-HULIS was formed in marine cloud water under moderately acidic conditions ($3.0 < pH_{HL-Fe} < 6.0$). The role of the complexation reaction of Fe with HULIS is the stabilization of L-Fe rather than the further promotion of Fe dissolution from aerosol particles. At present, thermodynamic data of HULIS with Fe in PM_{1.3} are not enough to evaluate the effects of HULIS on Fe dissolution. Therefore, further observations and laboratory experiments on the complex formation between HULIS and Fe are expected to improve our understanding of the effect of HULIS on Fe dissolution.

Data availability. The data are available upon request (Kohei Sakata, sakata.kohei@nies.go.jp).

Supplement. The supplement related to this article is available online at XXXX.

Author contributions. The study was designed by Kohei Sakata (K.S.), Hiroshi Tanimoto (H.T.), and Yoshio Takahashi (Yo.T.). Aerosol sampling was conducted by K.S., Aya Sakaguchi (A.S.), and Atsushi Matsuki (A.M.). Quantitative analyses were conducted by K.S., Minako Kurisu (M.K.), and Yo.T. XAFS experiments were conducted by K.S., M.K., Yo.T., Yusuke Tamenori (Yu. T.), and Yasuo Takeichi (Ya.T.). Single particle analyses were performed by K.S., Ya.T., and Yo. T. The model calculations were performed by K.S. The paper was written by K.S., H.T., and Yo.T. All authors were reviewed the manuscript.

Competing interests. The authors declare no competing interests.

Acknowledgements.

We thank all researchers and crews of KH-14-6 cruise to support our aerosol sampling. This study was supported by a Grant-in-Aid for the Japan Society for the Promotion of Science (JSPS) Fellows (Proposal No. 201801782), Research Institute for Oceanography Foundation (Kyoto, Japan, Proposal No. H30-R4), and the Cooperative Research Program of the Institute of Nature and Environmental Technology, Kanazawa University (Proposal No. 19002). XAFS experiments were approved by KEK-PF (2013S2-003, 2015S2-002, 2016G632, 2018S1-001, 2019G093) and SPring-8 (2015A1809 and 2016A1642).

Figure captions

670 Figure 1: Track chart of the research cruise of KH-14-6 (R/V Hakuho-Maru) and sampling locations of WPO, CPO and SPO samples. Red circle showed the locations of Beijing and Noto Ground-Based Research Observatory (NOTOGRO). The figure was described using Ocean Data View (Schlitzer, 2021).

Figure 2: Iron K-edge (a) XANES and (b) EXAFS spectra of reference materials.

675 Figure 3: (a) total Fe (ng/m³), (b) labile Fe (ng/m³), (c) Fe_{sol}%, (d) EF of Fe, (e) total Al (ng/m³), (f) labile Al (ng/m³), and (g) Al_{sol}% in TSP.
~~Figure 1: Track chart of the research cruise of KH-14-6 (R/V Hakuho-Maru) and sampling locations of WPO, CPO and SPO samples. Red circle showed the locations of Beijing and Noto Ground-Based Research Observatory (NOTOGRO).~~

~~Figure 2: Backward trajectories of (a) WPO1, (b) WPO2, (c) WPO3, (d) CPO, and (e) SPO obtained by the ensemble mode. The backward trajectories were calculated at midpoint of each sampling region shown in Fig. S1. Duration of WPO1 to WPO3 were 5 days, where those for CPO and SPO samples were 7 days.~~

680 ~~Figure 3: (a) total Fe (ng/m³), (b) labile Fe (ng/m³), (c) Fe_{sol}%, (d) EF of Fe, (e) total Al (ng/m³), (f) labile Al (ng/m³), and (g) Al_{sol}% in TSP.~~

Figure 4: Size distributions of (a) total Fe (ng/m³), (b) labile Fe (ng/m³), (c) Fe_{sol}%, (d) total Al (ng/m³), (e) labile Al (ng/m³), and (f) Al_{sol}%. The PM_{1.3} is shown in yellow regions.

~~The PM_{1.3} is shown in yellow regions.~~

685 ~~Figure 5: Scatter plots of Fe_{sol}% with (a) EF of V, (b) EF of Ni, (c) EF of Pb, and (d) nss-SO₄²⁻. (e) the scatter plot between nss-SO₄²⁻ and EF of Pb. (f) the scatter plot of residuals of EF of Pb and Fe_{sol}%.~~

Figure 6: (a) A scatter plot between Fe_{sol}% and [H⁺]_{mineral}. The blue region shows positive [H⁺]_{mineral}. Size distributions of (b) [H⁺]_{mineral} and (c) nss-Ca²⁺. The PM_{1.3} is shown in yellow regions.

690 ~~Figure 7: (a) Fraction of Fe species in each sample determined by Fe K-edge XANES spectroscopy. (b) Fe K-edge XANES spectra of reference materials. Colored spectra were used as reference materials for LCF, whereas black spectra were not assigned as dominant Fe species in our samples. Iron K-edge XANES spectra of size-fractionated aerosol particles collected in (e) WPO2 and (f) NOTOGRO. (d) a scatter plot between fraction of Fe(III)-HULIS and Fe_{sol}%.~~

695 ~~Figure 8: Al K-edge XANES spectra of (a) WPO2 and (b) WPO3. Black and red solid line showed XANES spectra for aerosol particles and fitting spectra, respectively. Colored spectra with dashed line show fitting components. The Al K-edge XANES spectra of particle 1 to particle % in PM_{1.3} in panel (a) were obtained by single particle analysis using STXM. The X ray image of these particles are shown in Figure 9.~~

Figure 8: Al K-edge XANES spectra of (a) WPO2 and (b) WPO3. Black and red solid line showed XANES spectra for aerosol particles and fitting spectra, respectively. Colored spectra with dashed line show fitting components. Figure 8: (a 1 and b 1) X ray image at post edge of C K-edge of single aerosol particles in S6 WPO2. (a 2 and b 2) RGB

700 composites of Fe (R: red), carboxylates (G: green), and Na (B: blue). Distributions of carboxylates (OCs), K, Fe, Na, and Al are shown in panels (a-3 and b-3), (a-4 and b-4), (a-5 and b-5), (a-6 and b-6), and (a-7 and b-7), respectively. (a-8 and b-8) Carbon K-edge XANES spectra on the surface of each phyllosilicate particle. Particle 1 in panel (a) was covered with tiny amounts of OCs, whereas particles 2 and 3 in panel b is covered with aliphatic C. Gray, light green, pink, light blue, orange, and brown regions show the peak positions of aromatic C, ketonic C, aliphatic C, carboxylates, carbonate, and potassium, respectively.

705 The relative abundance of species identified by LCF are shown in the parentheses beside the sample name (i.e., Gibbsite (20%) for S5-WPO2).

710 Figure 9: (a and c) dissolution curves for each Fe pool (colored dashed lines) and summation of all Fe pools (solid black line) in S6-WPO2 and S6-WPO3 as a function of dissolution time. Solid red line in these figures shows the observed L-Fe concentrations. The pH was set so that the total value reached the observed L-Fe in approximately ~~6090~~ 6090 h (expected time for wet aerosol phase). (b and d) pH dependences of L-Fe species in ALW for S6-WPO2 and S6-WPO3. Pink and yellow regions show the aerosol pH for the proton-promoted dissolution (same pH as in panels a and c) and stable pH regions of Fe(III)-HULIS, respectively.

Figure 10: The schematic of alteration processes of Fe in phyllosilicate particles in PM_{1.3} during transport.

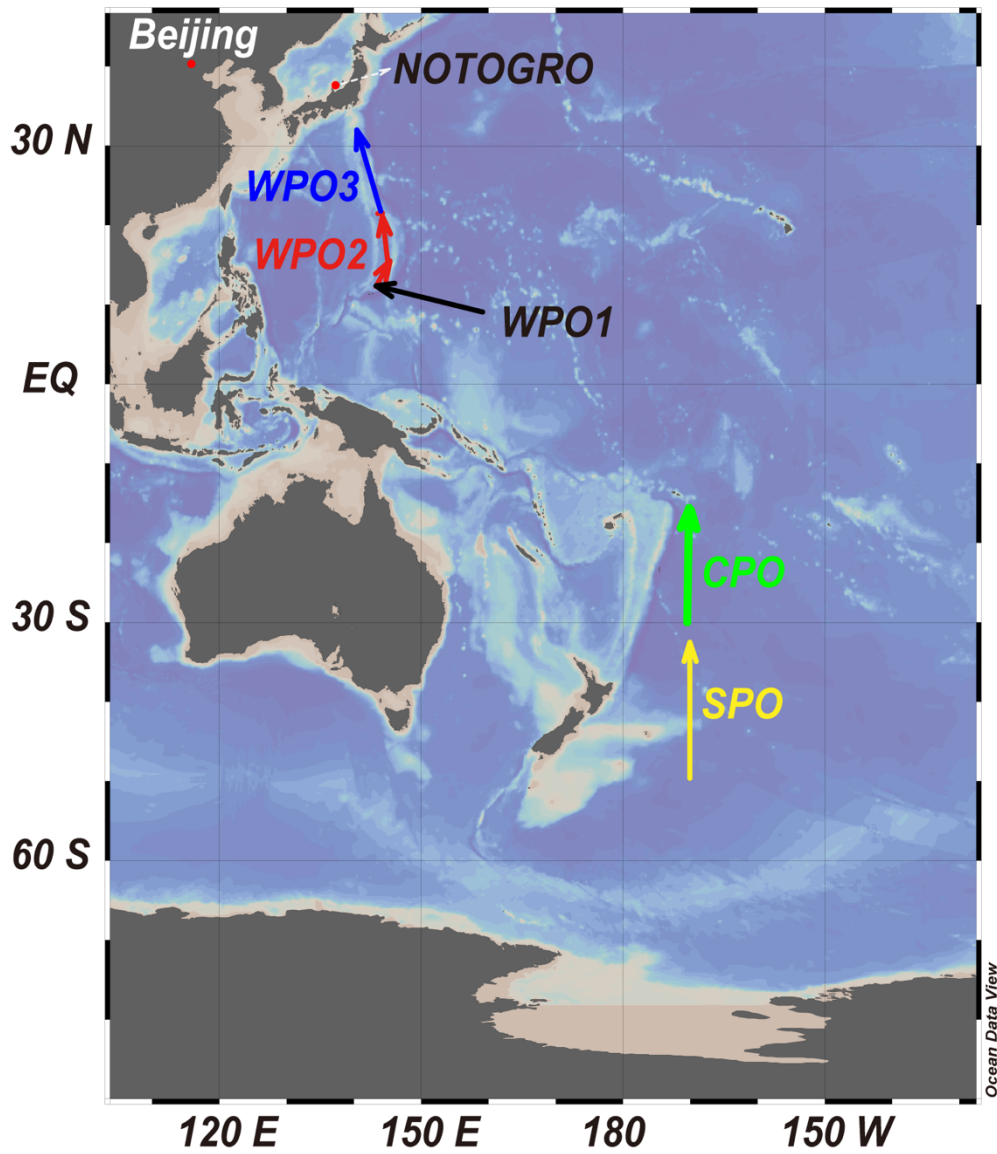
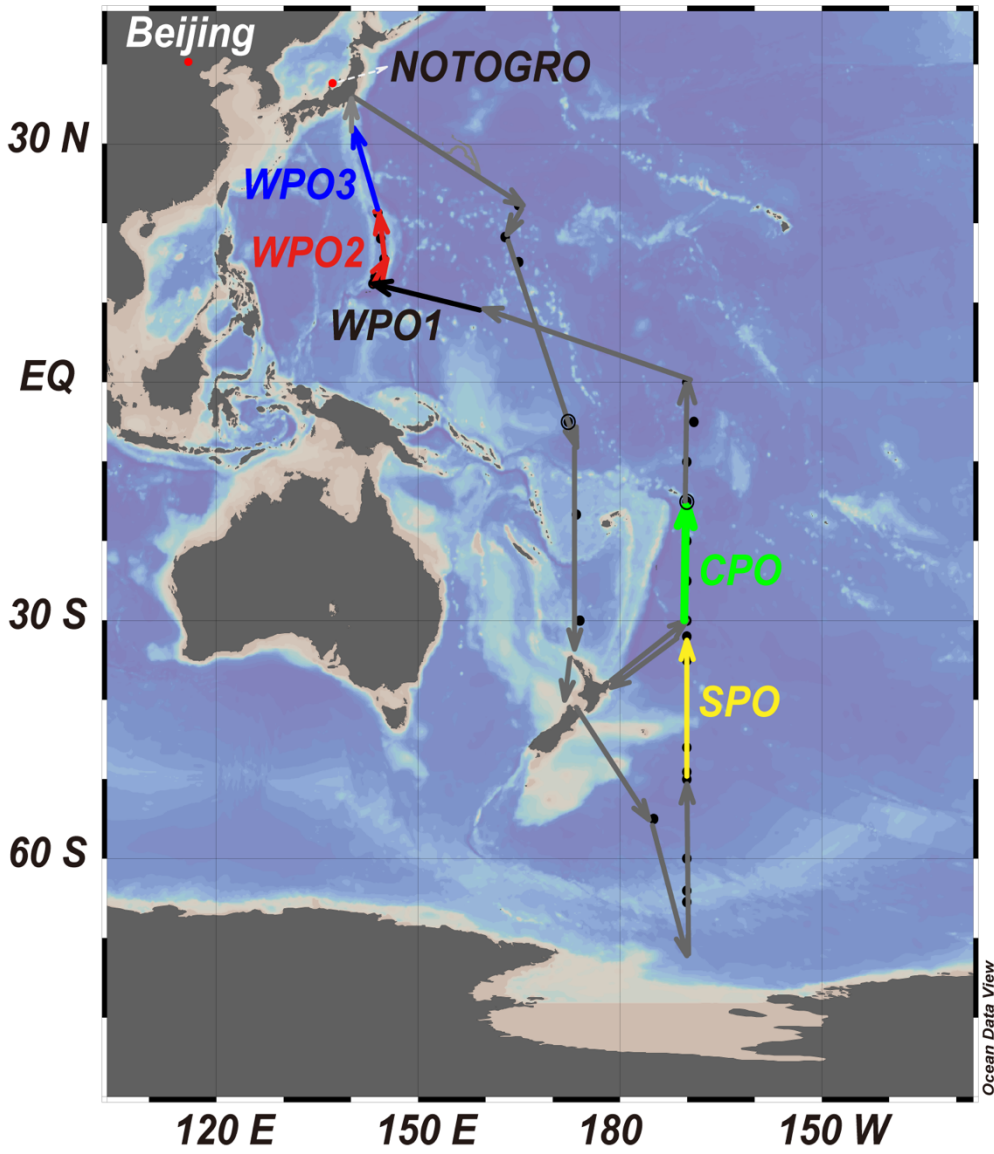


Figure 1: Track chart of the research cruise of KH-14-6 (R/V Hakuho-Maru) and sampling locations of WPO, CPO and SPO samples. Red circle showed the locations of Beijing and Noto Ground-Based Research Observatory (NOTOGRO).



725

The figure was described using Ocean Data View (Schlitzer, 2021).

Figure 1: Track chart of the research cruise of KH 14-6 (R/V Hakuho Maru) and sampling locations of WPO, CPO and SPO samples. Red circle showed the locations of Beijing and Note Ground Based Research Observatory (NOTOGRO). The figure was described using Ocean Data View (Schlitzer, 2021).

730

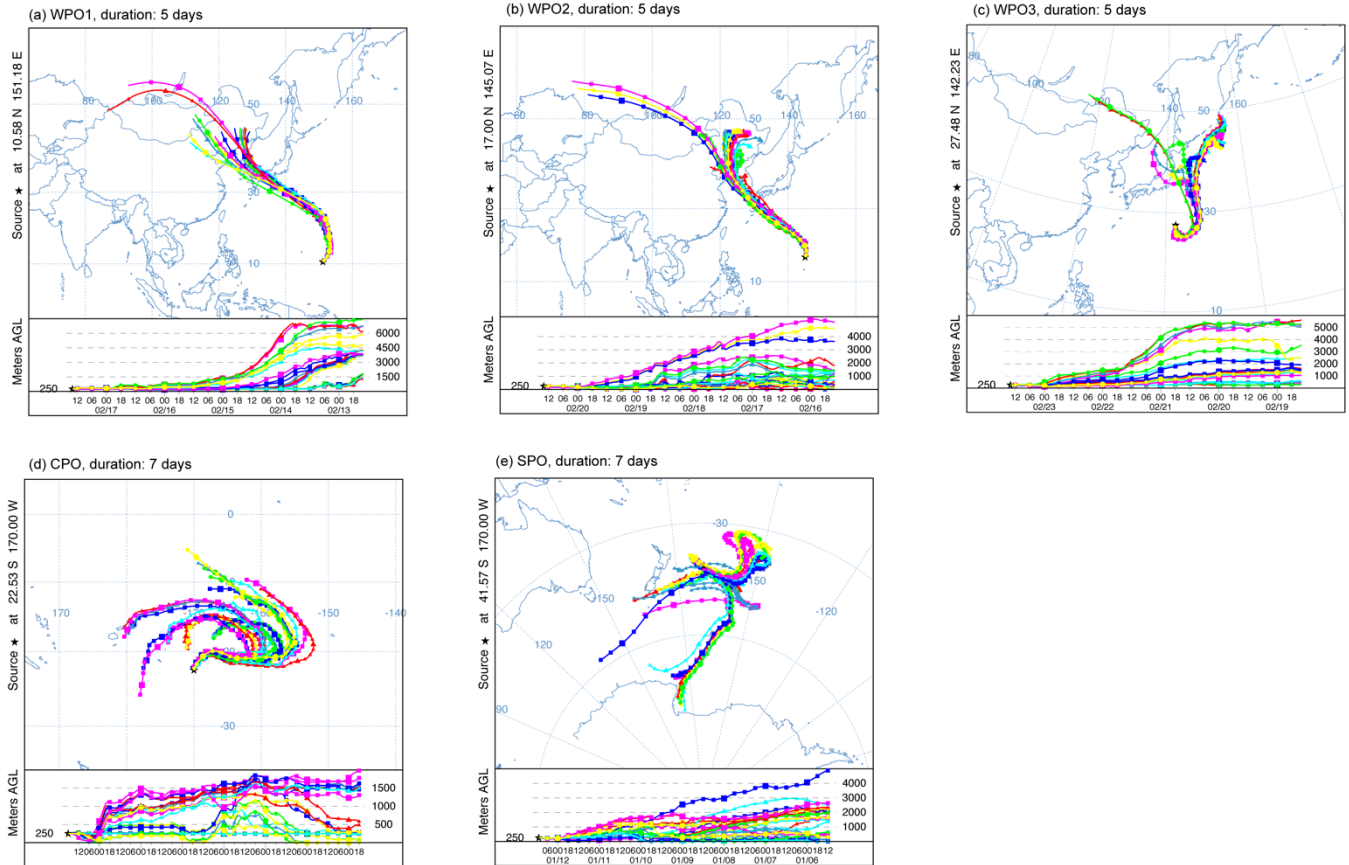
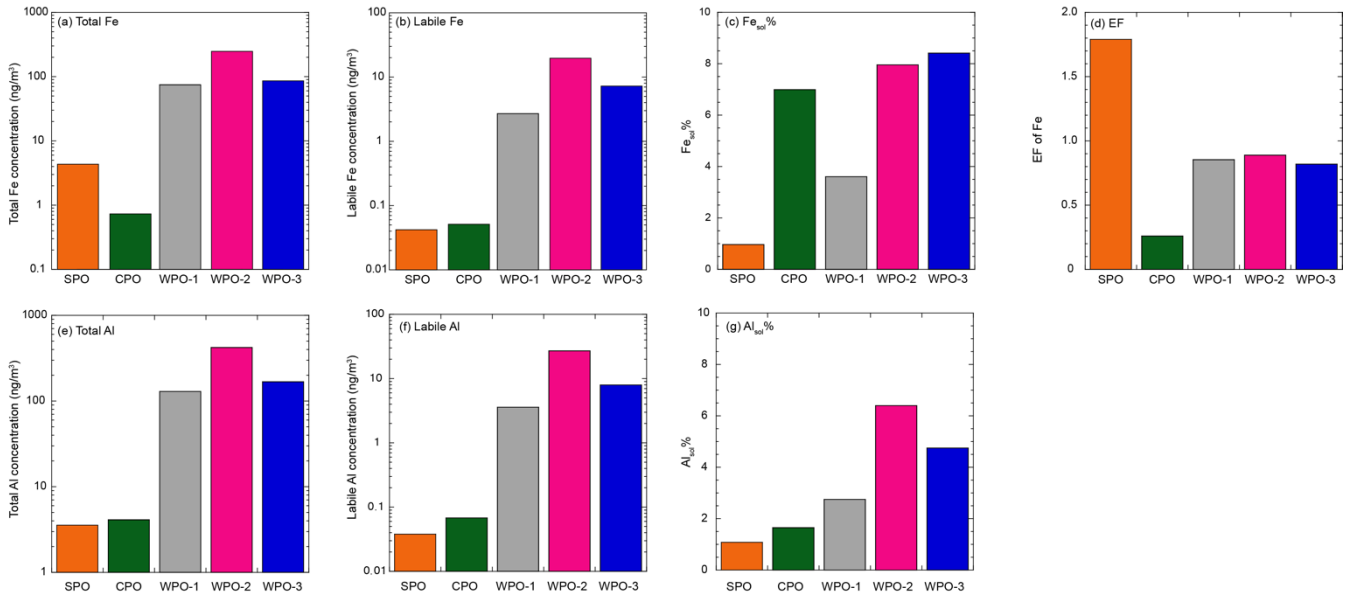


Figure 2: Backward trajectories of (a) WPO1, (b) WPO2, (c) WPO3, (d) CPO, and (e) SPO obtained by the ensemble mode. The backward trajectories were calculated at midpoint of each sampling region shown in Fig. S1. Duration of WPO1 to WPO3 were 5 days, where those for CPO and SPO samples were 7 days.

745

750



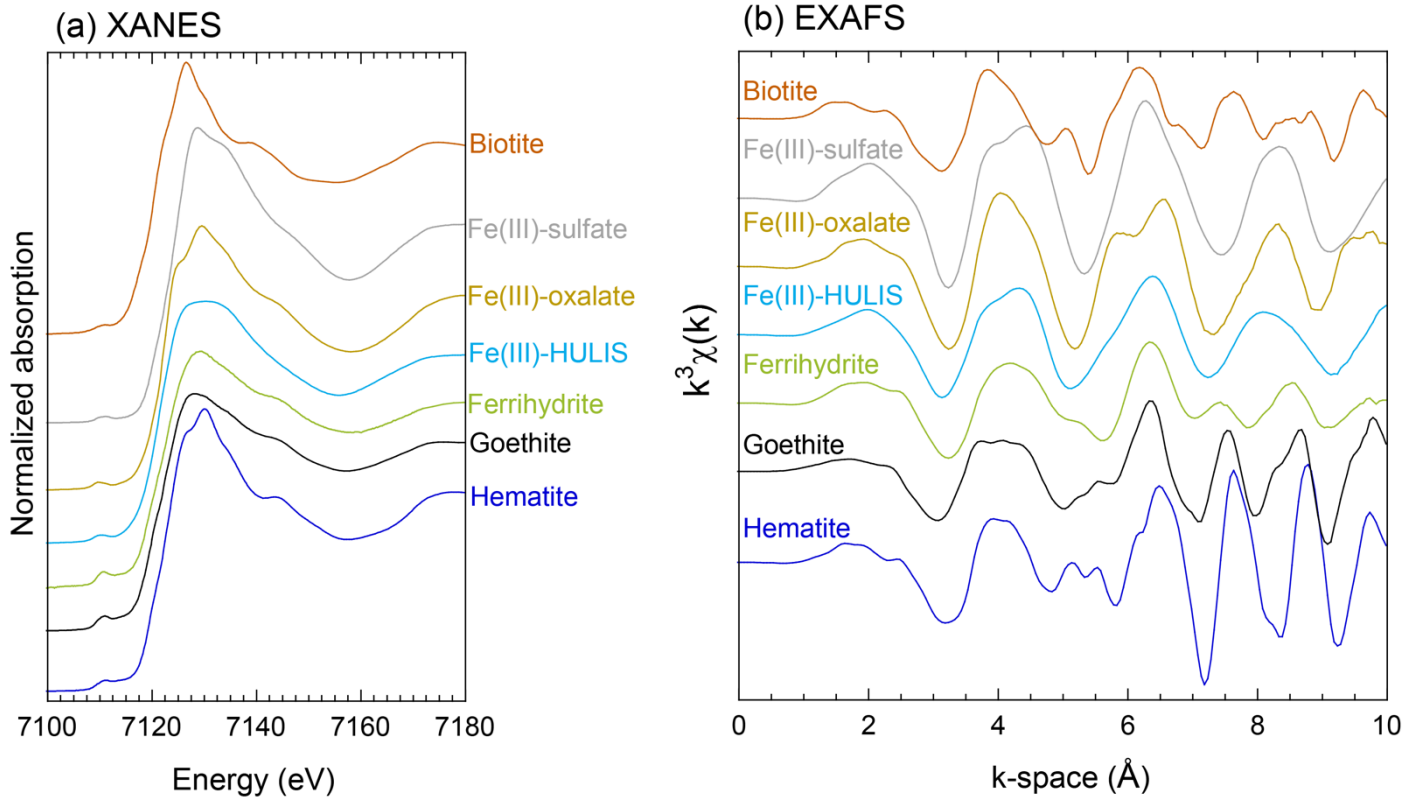


Figure 2: Iron K-edge (a) XANES and (b) EXAFS spectra of reference materials.

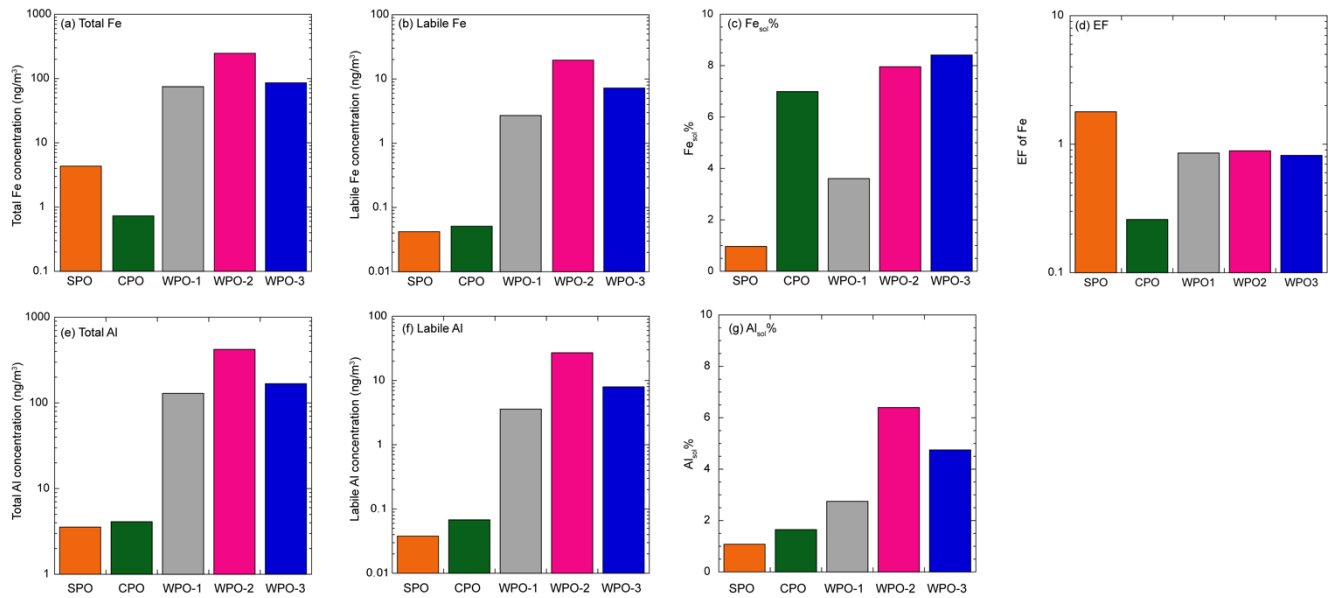


Figure 3: (a) total Fe (ng/m³), (b) labile Fe (ng/m³), (c) Fe_{sol}%, (d) EF of Fe, (e) total Al (ng/m³), (f) labile Al (ng/m³), and (g) Al_{sol}% in TSP.

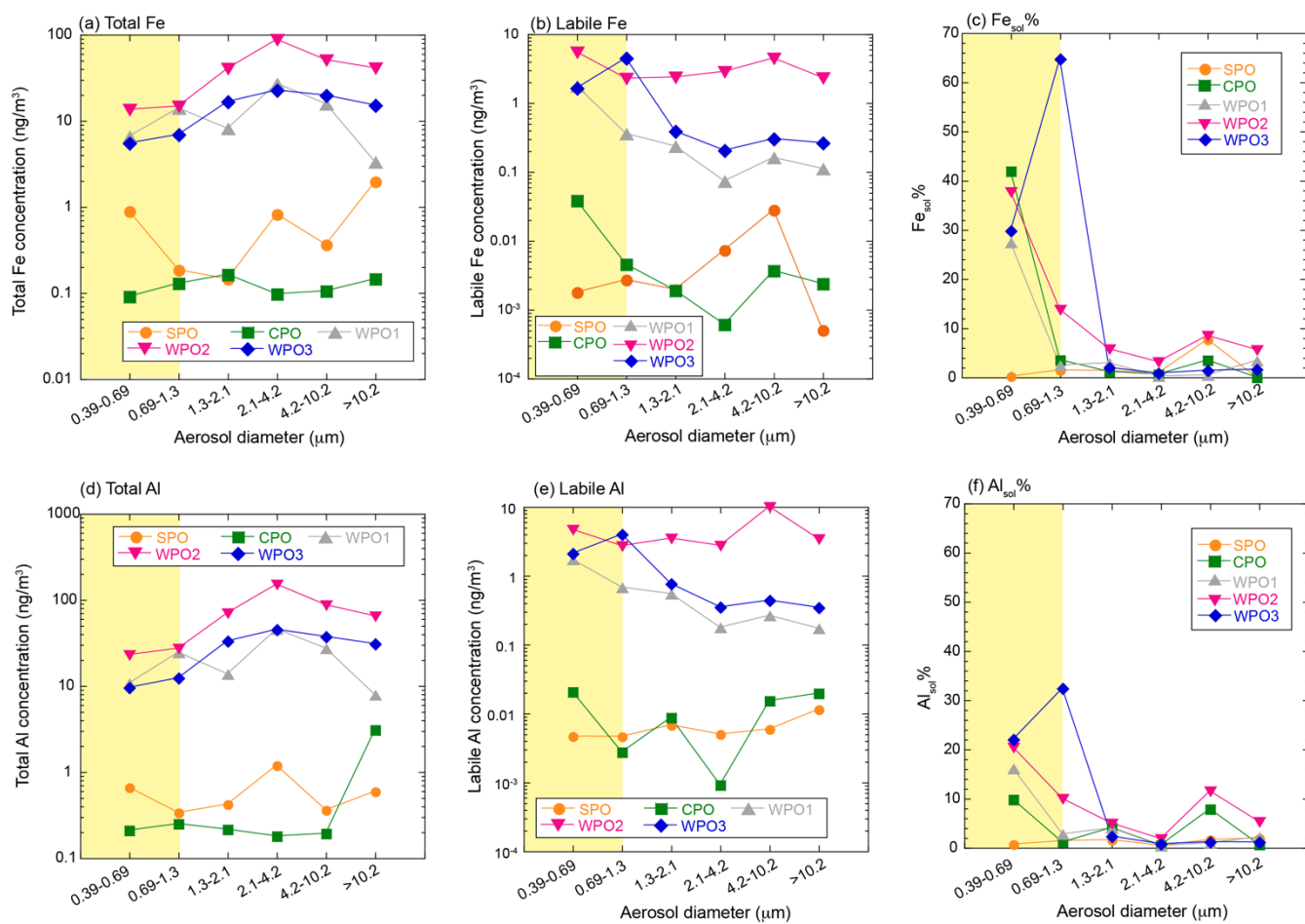


Figure 4: Size distributions of (a) total Fe (ng/m³), (b) labile Fe (ng/m³), (c) Fe_{sol}%, (d) total Al (ng/m³), (e) labile Al (ng/m³), and (f) Al_{sol}%. The PM_{1.3} is shown in yellow regions.

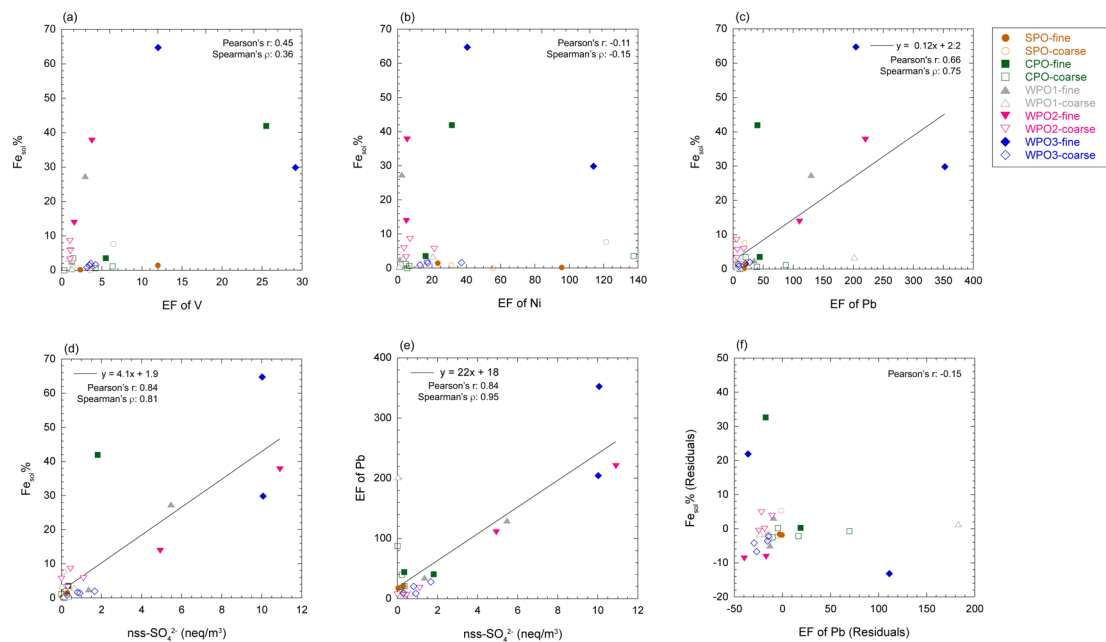
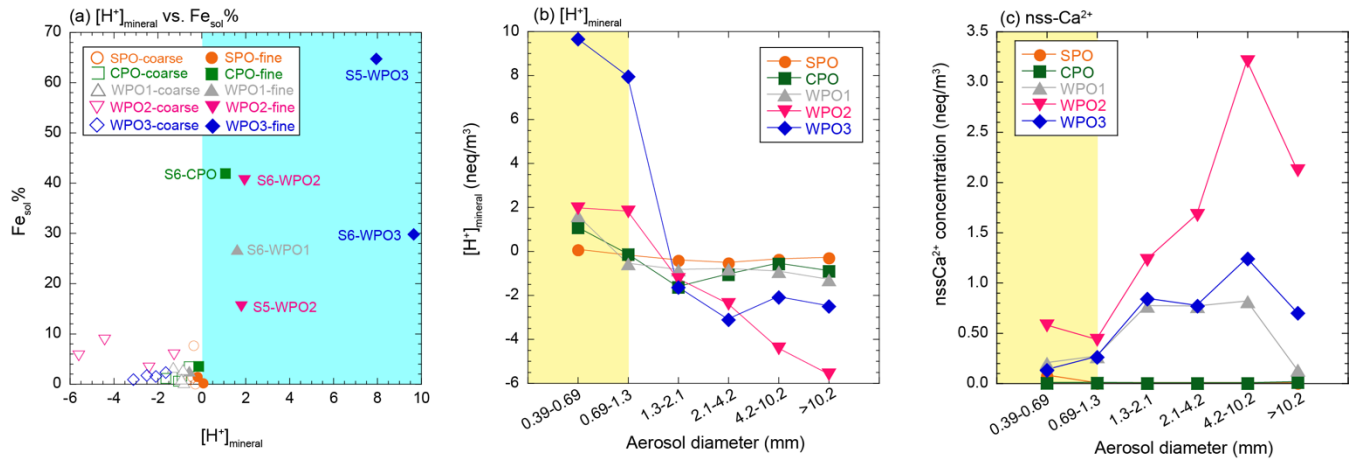
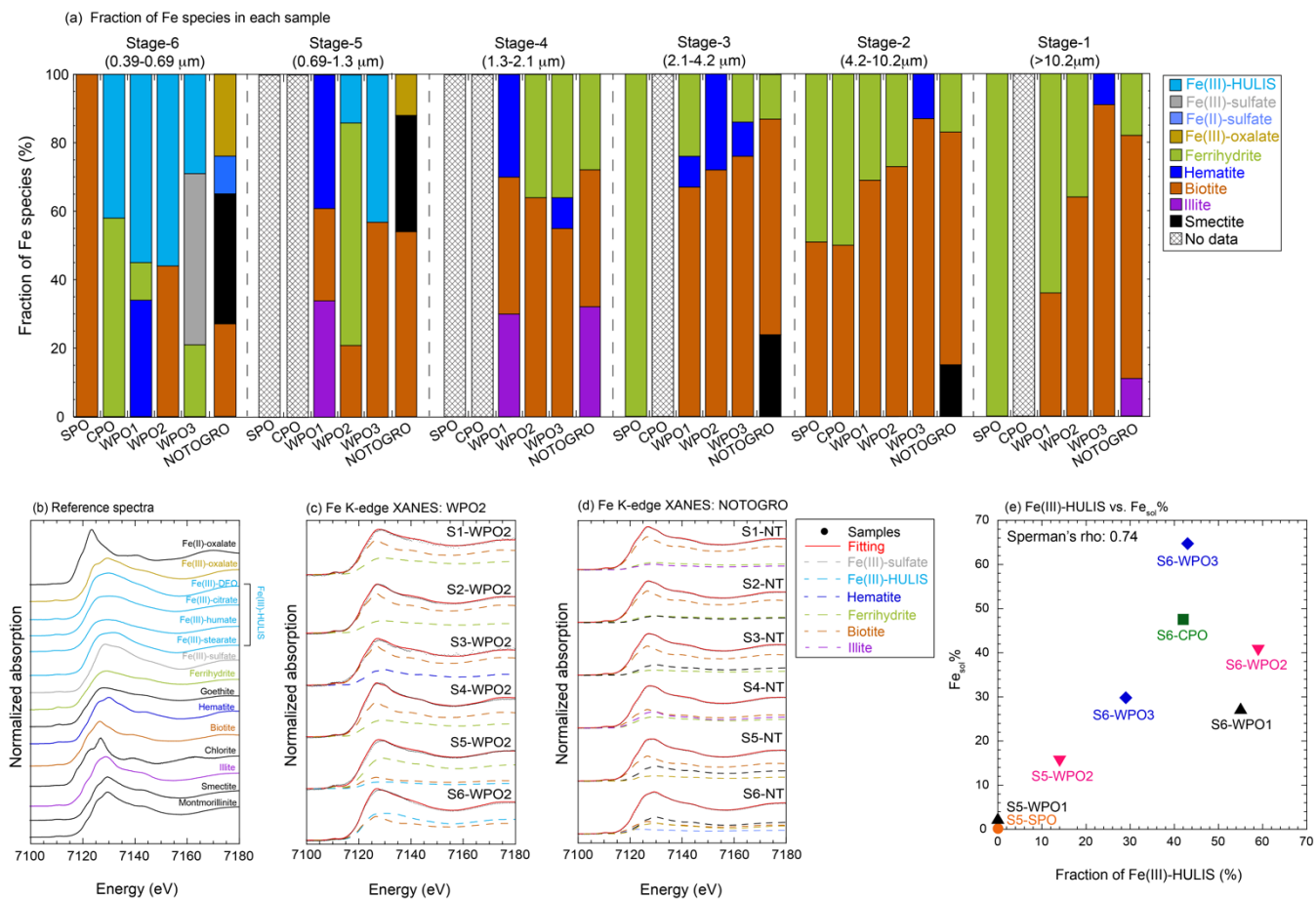


Figure 5: Scatter plots of $Fe_{sol}\%$ with (a) EF of V, (b) EF of Ni, (c) EF of Pb, and (d) $nss-SO_4^{2-}$. (e) the scatter plot between $nss-SO_4^{2-}$ and EF of Pb. (f) the scatter plot of residuals of EF of Pb and $Fe_{sol}\%$.



790 Figure S6: (a) A scatter plot between $Fe_{\text{sol}}\%$ and $[H^+]_{\text{mineral}}$. The blue region shows positive $[H^+]_{\text{mineral}}$. Size distributions of (b) $[H^+]_{\text{mineral}}$ and (c) $nss-Ca^{2+}$. The $PM_{1.3}$ is shown in yellow regions.



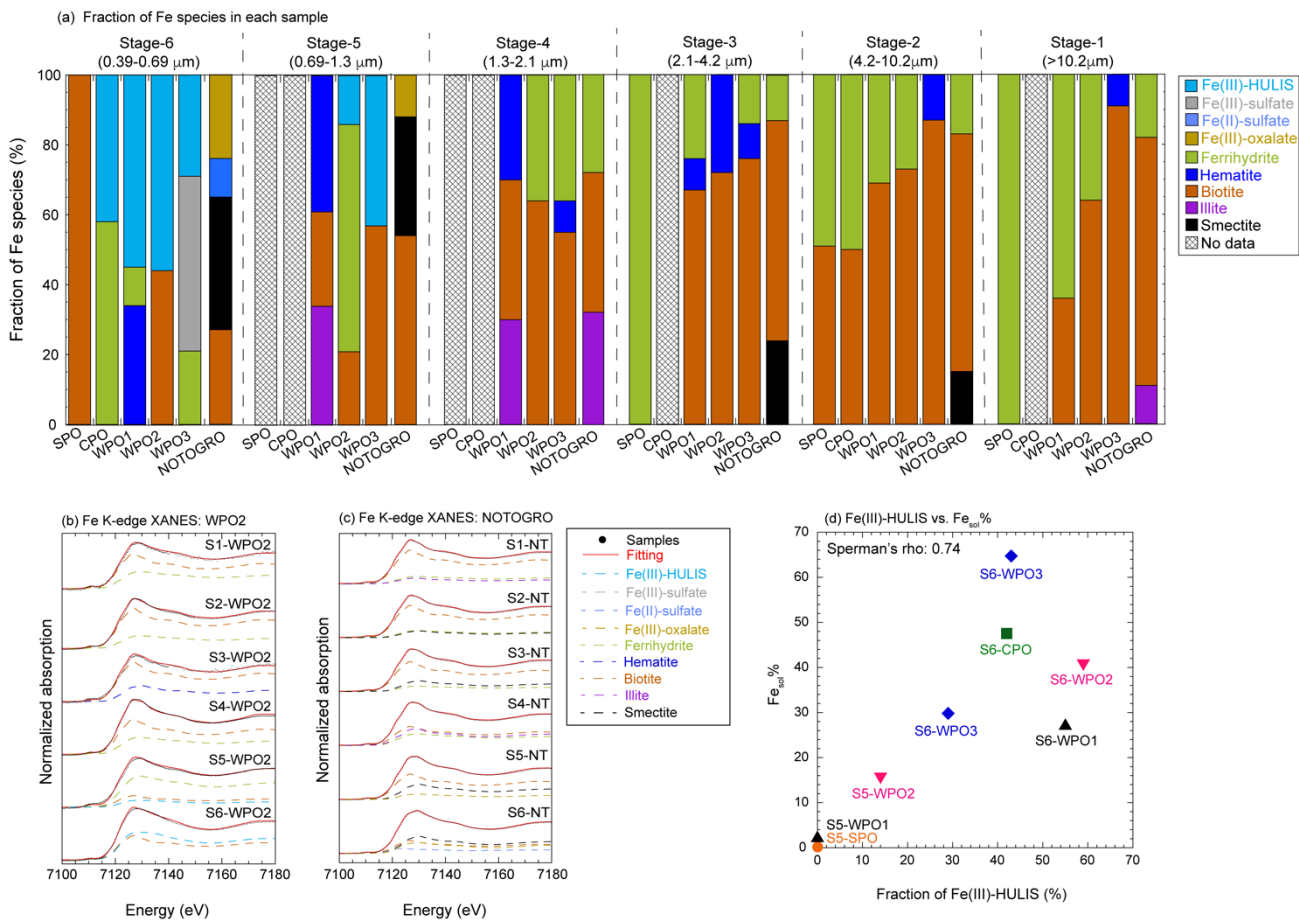
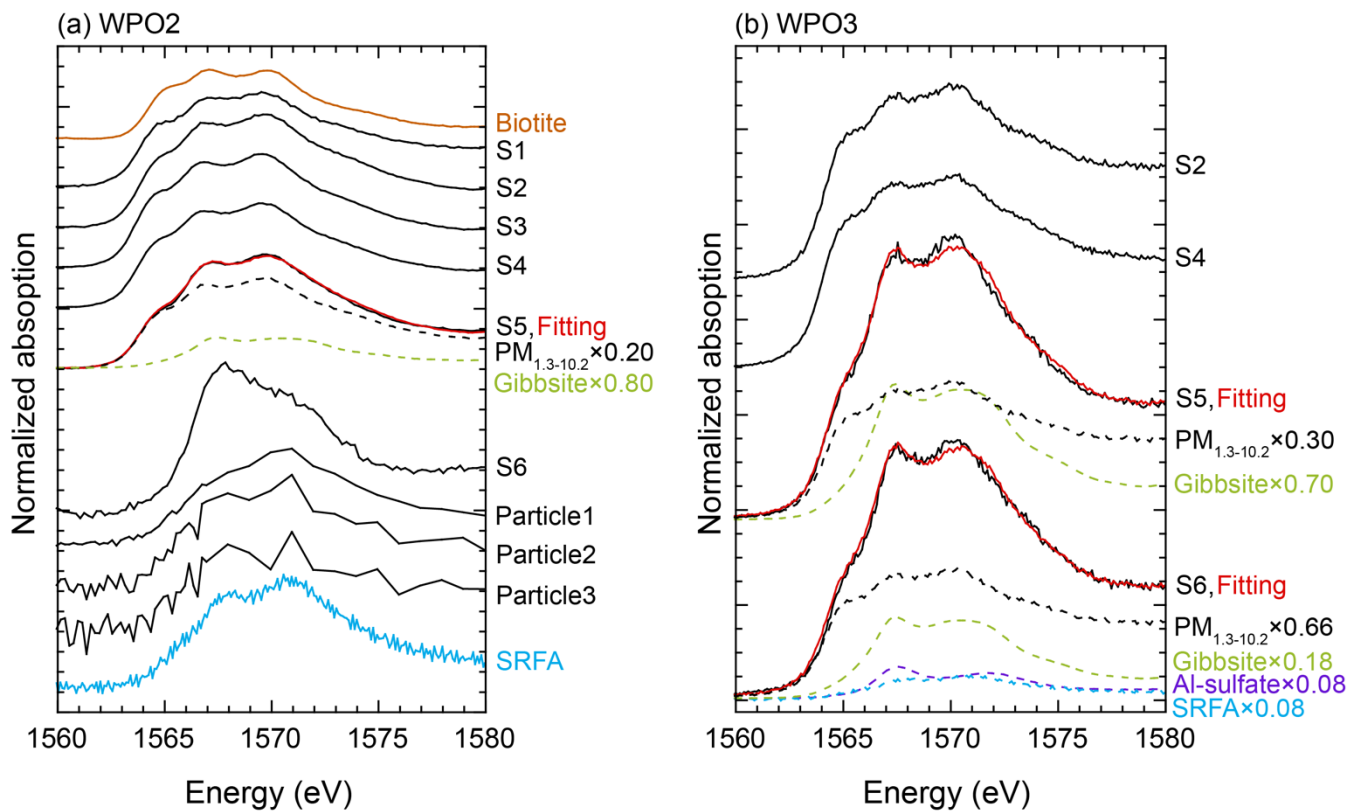
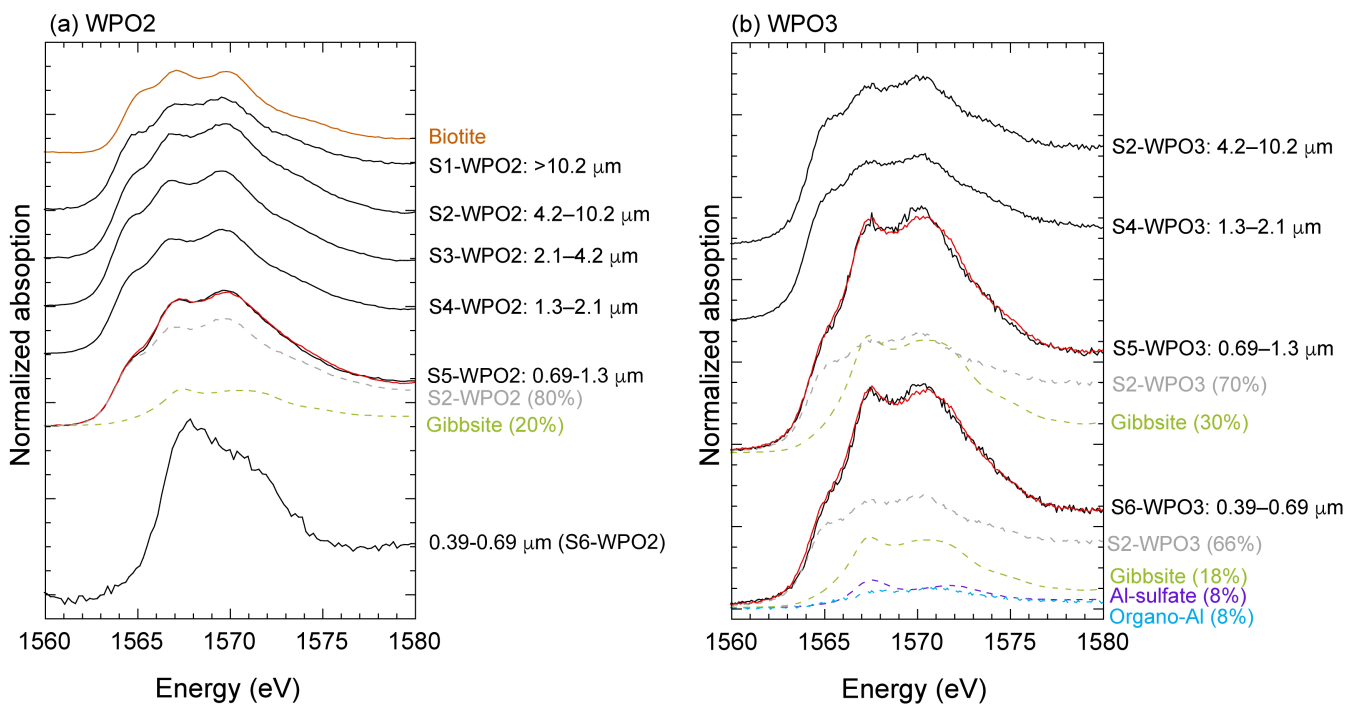


Figure 67: (a) Fraction of Fe species in each sample determined by Fe K-edge XANES spectroscopy. (b) Fe K-edge XANES spectra of reference materials. Colored spectra were used as reference materials for LCF, whereas black spectra were not assigned as dominant Fe species in our samples. (c) Fe K-edge XANES spectra of size-fractionated aerosol particles collected in (b) WPO2 and their fitting components. (d) a scatter plot between fraction of Fe(III)-HULIS and $\text{Fe}_{\text{sol}}\%$.



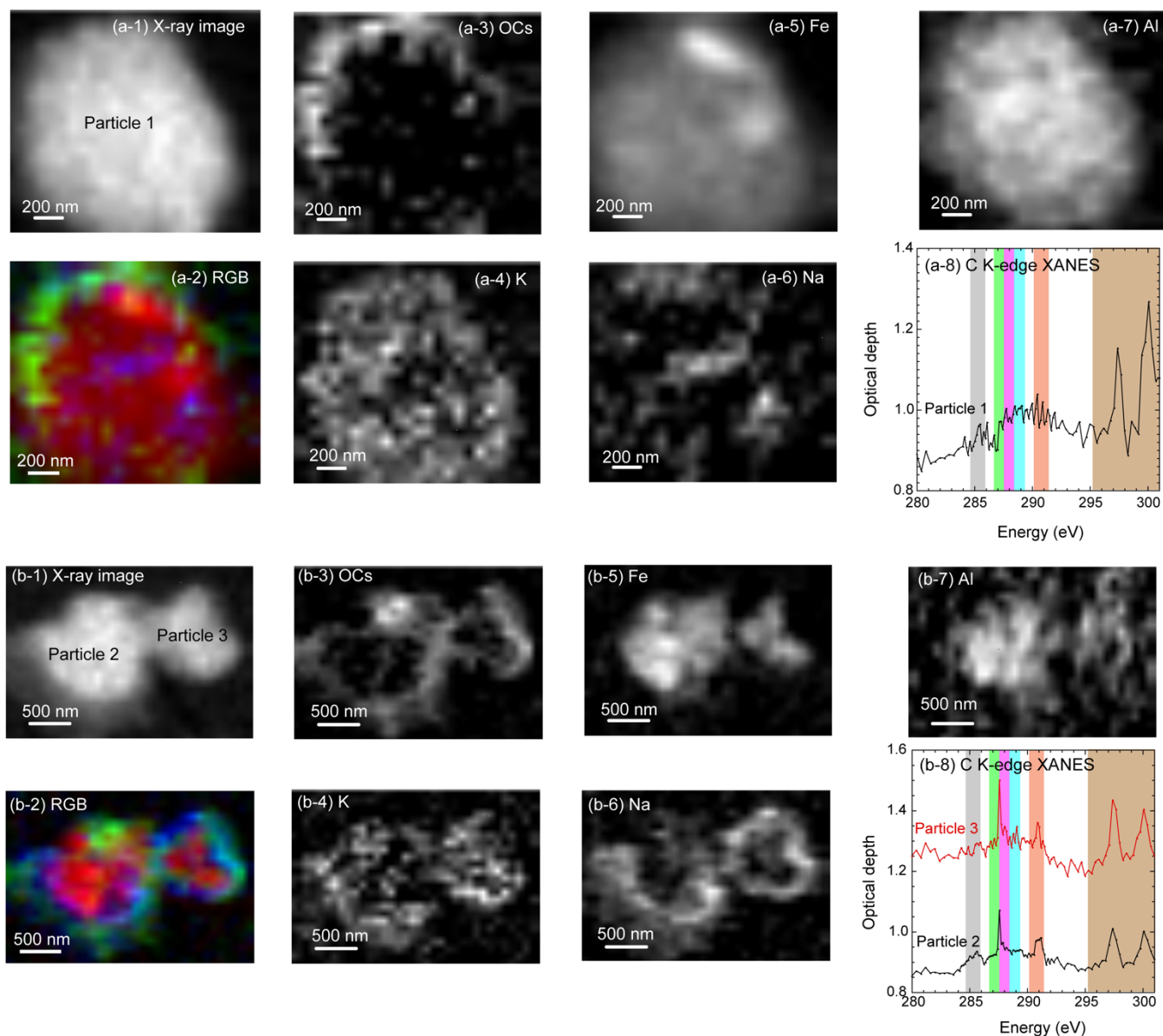
% in PM₁.

810 ~~Figure 7 Al K-edge XANES spectra of (a) WPO2 and (b) WPO3. Black and red solid line showed XANES spectra for aerosol particles and fitting spectra, respectively. Colored spectra with dashed line show fitting components. The Al K-edge XANES spectra of particle 1 to particle 3 in panel (a) were obtained by single particle analysis using STXM. The X-ray image of these particles are shown in Figure 9.~~



820

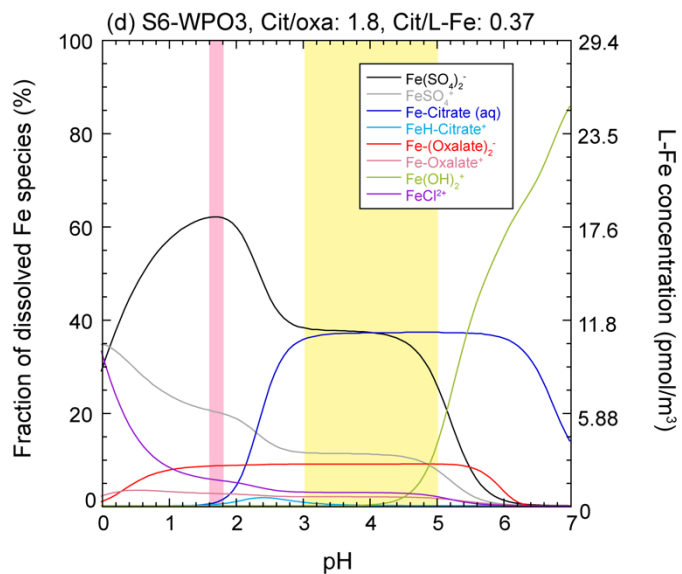
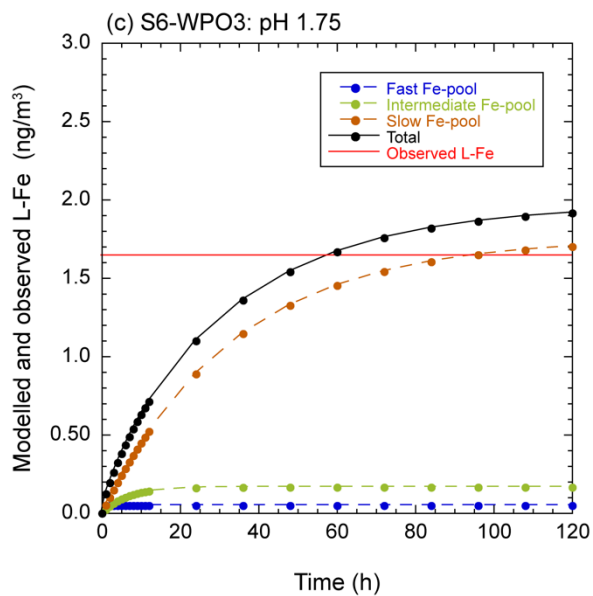
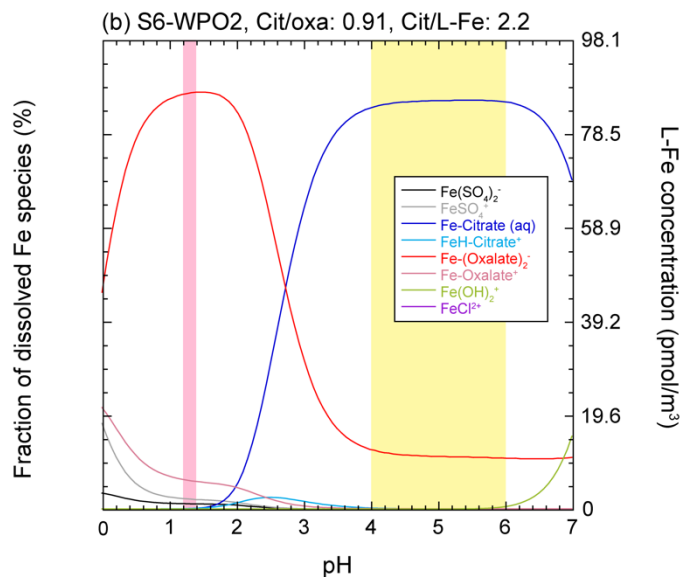
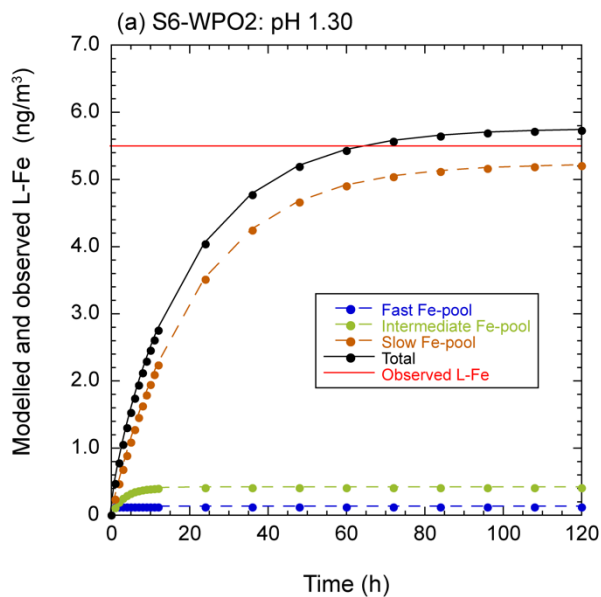
Figure 8: Al K-edge XANES spectra of (a) WPO2 and (b) WPO3. Black and red solid line showed XANES spectra for aerosol particles and fitting spectra, respectively. Colored spectra with dashed line show fitting components.



825

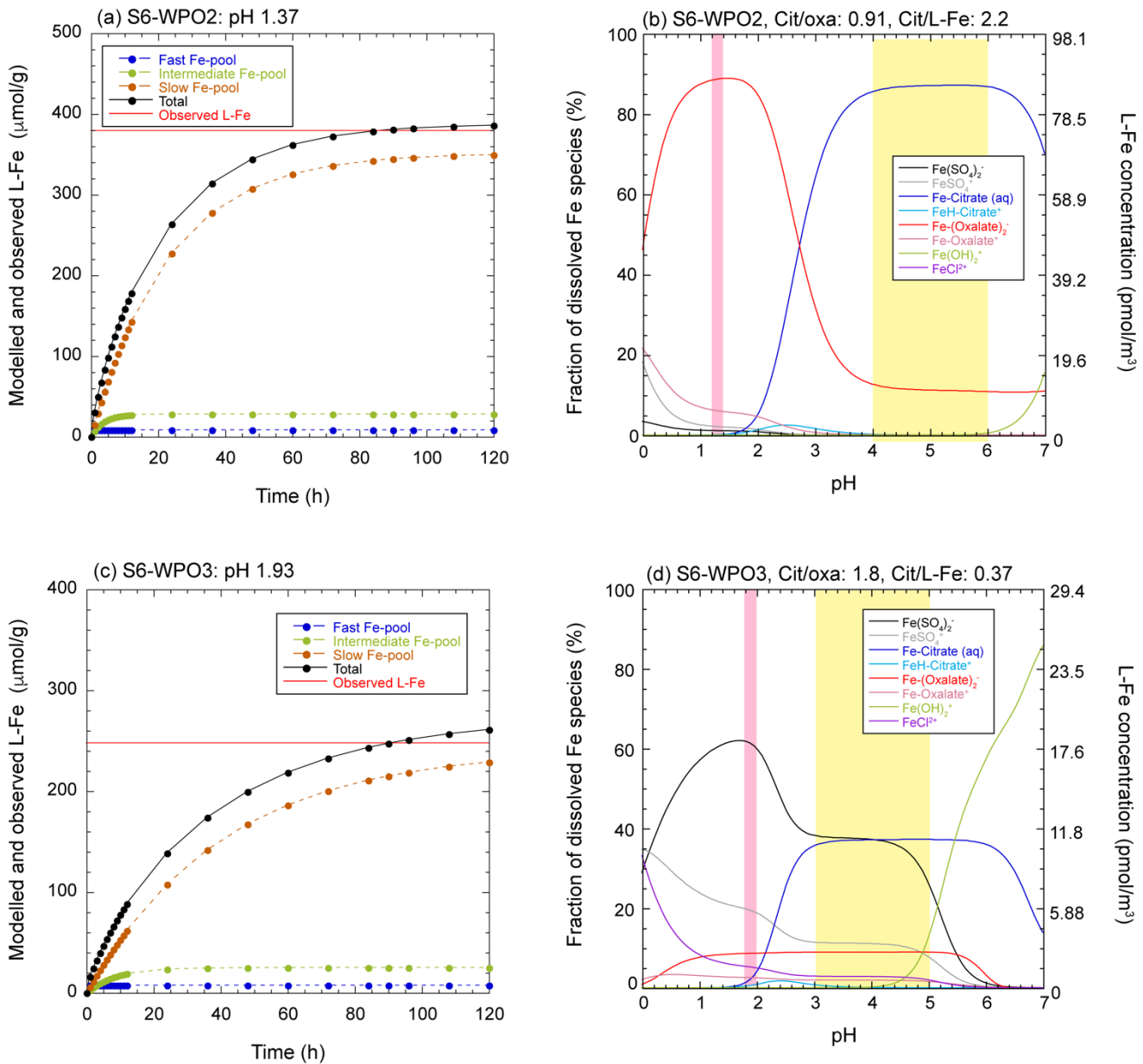
Figure 8 (a 1 and b 1) X ray image at post edge of C K edge of single aerosol particles in S6-WPO2. (a 2 and b 2) RGB composites of Fe (R: red), carboxylates (G: green), and Na (B: blue). Distributions of carboxylates (OCs), K, Fe, Na, and Al are shown in panels (a 3 and b 3), (a 4 and b 4), (a 5 and b 5), (a 6 and b 6), and (a 7 and b 7), respectively. (a 8 and b 8) Carbon K edge XANES spectra on the surface of each phyllosilicate particle. Particle 1 in panel (a) was covered with tiny amounts of OCs, whereas particles 2 and 3 in panel b is covered with aliphatic C. Gray, light green, pink, light blue, orange, and brown regions show the peak positions of aromatic C, ketonic C, aliphatic C, carboxylates, carbonate, and potassium, respectively.

830



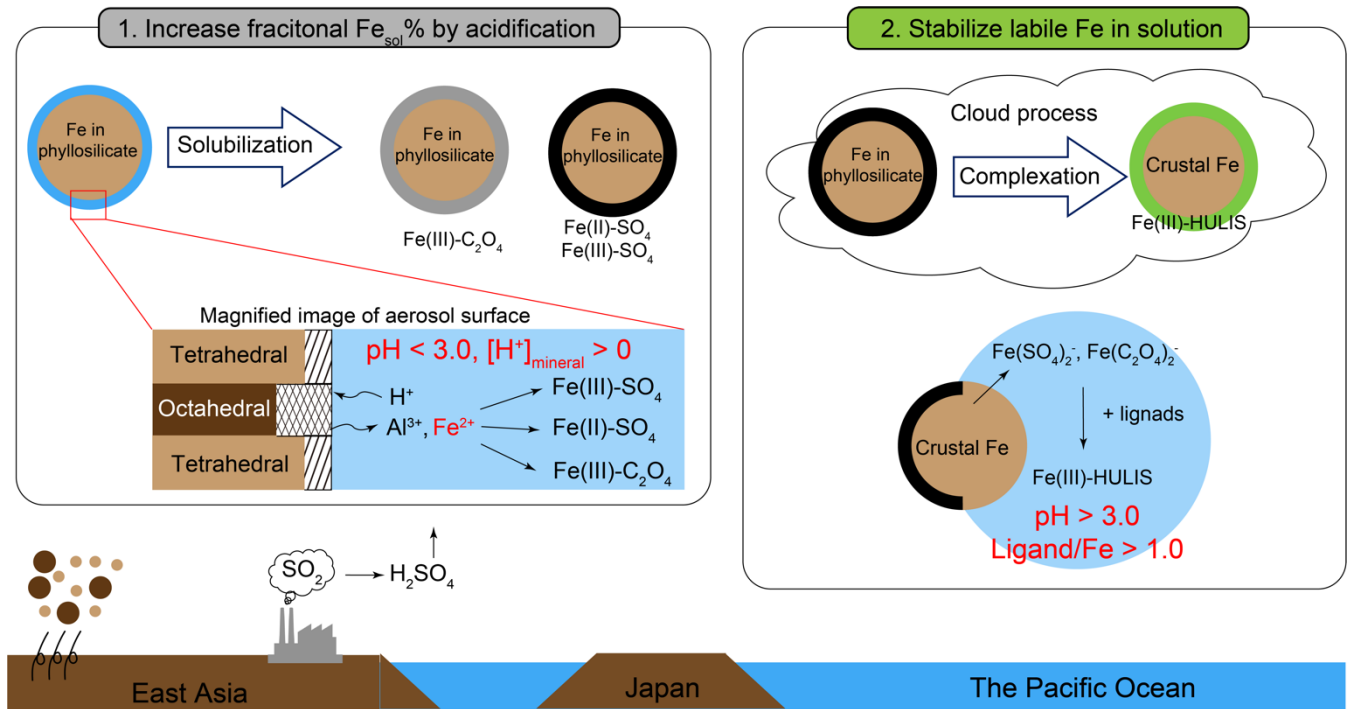
835

-The relative abundance of species identified by LCF are shown in the parentheses beside the sample name (i.e., Gibbsite (20%) for S5-WPO2).



840 Figure 9: (a and c) dissolution curves for each Fe pool (colored dashed lines) and summation of all Fe pools (solid black line) in S6-WPO2 and S6-WPO3 as a function of dissolution time. Solid red line in these figures shows the observed L-Fe concentrations. The pH was set so that the total value reached the observed L-Fe in approximately 6090 h (expected time for wet aerosol phase). (b and d) pH dependences of L-Fe species in ALW for S6-WPO2 and S6-WPO3. Pink and yellow regions show the aerosol pH for the proton-promoted dissolution (same pH as in panels a and c) and stable pH regions of Fe(III)-HULIS, respectively.

845



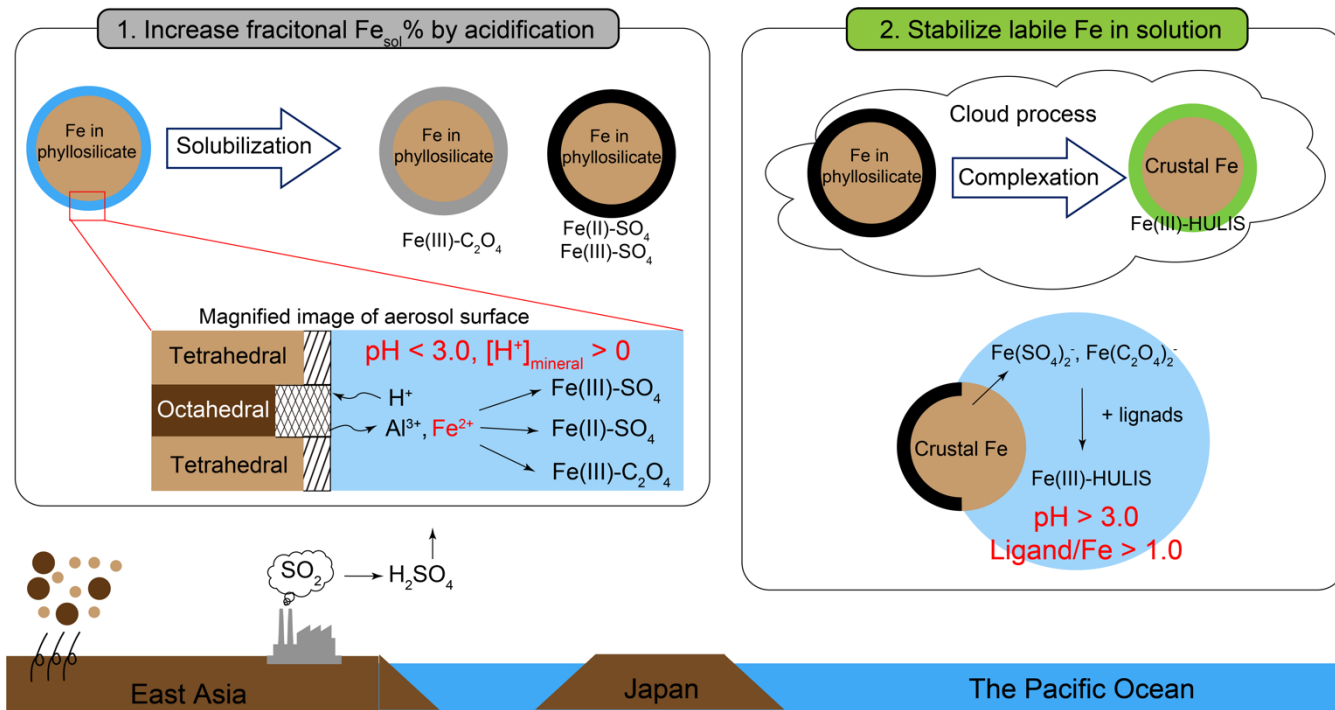


Figure 10: The schematic of alteration processes of Fe in phyllosilicate particles in PM_{1.3} during transport.

Table 1. Model parameter for three Fe-pool model.

	pH _{PPD}	Expected Fe species	%Fe(0)	Dissolution rate
Fast	1.0–2.0	Ferrihydrite	Fixed at 0.9	$\log k_{\text{fast}} = -0.50 \text{ pH}_{\text{PPD}} + 1.87$
	2.0–3.0	Poor crystalline Fe-oxides	$\% \text{FeT} = -0.4 \text{ pH}_{\text{PPD}} + 1.7$	
Intermediate	1.0–2.0	nano-size Fe-oxides	Fixed at 3.0	$\log k_{\text{intermediate}} = -0.66 \text{ pH}_{\text{PPD}} + 0.36$
	2.0–3.0		$\% \text{FeT} = -2.0 \text{ pH}_{\text{PPD}} + 7.0$	
Slow	1.0–2.0	Crystalline Fe-oxides	$\% \text{FeT} = -15.2 \text{ pH}_{\text{PPD}} + 58.4$	$\log k'_{\text{slow}} = -0.44 \text{ pH}_{\text{PPD}} - 0.76$
	2.0–3.0	Fe in clay mineral		

References

- Abualhaija, M. M., Whitby, H., and van den Berg, C. M. G.: Competition between copper and iron for humic ligands in estuarine waters, *Mar. Chem.*, 172, 46–56, <http://dx.doi.org/10.1016/j.marchem.2015.03.010>, 2015.
- Adachi, K., Oshima, N., [Gong, Z., de Sá, S., Bateman, A. P., Martin, S. T., de Brito, J. F., Artaxo, P., Cirino, G. G., Sedlacek III, A. J., Buseck, P. R.: Mixing states of Amazon basin aerosol particles transported over long distances using transmission electron microscopy. *Atmos. Chem. Phys.*, 20, 11923–11939, <https://doi.org/10.5194/acp-20-11923-2020>, 2020.](#)
- [Adachi, K., Oshima, N., Ohata, S., Yoshida, A., Moteki, N., and Koike, M.: Compositions and mixing states of aerosol particles by aircraft observations in the Arctic springtime, 2018, *Atmos. Chem. Phys.*, 21, 3607–3626, <https://doi.org/10.5194/acp-21-3607-2021>, 2021.](#)
- Al-Abadleh, H. A.: Review of the bulk and surface chemistry of iron in atmospherically relevant systems containing humic-like substances, *RSC Adv.*, 5, 45785, <https://doi.org/10.1039/C5RA03132J>, 2015.
- [Amrani, A., Said-Ahmad, W., Shaked, Y., and Kiene, R. P.: Sulfur isotope homogeneity of oceanic DMSP and DMS, *Proc. Natl. Acad. Sci. U.S.A.*, 110, 18413–18418, <https://doi.org/10.1073/pnas.1312956110>, 2013.](#)
- Angle, K. J., Crocker, D. R., Simpson, R. M. C., Mayer, J. J., Garofalo, L. A., Moore, A. N., Mora Garcia, S. L., Or, V. W., Srinivasan, S., Farhan, M., Sauer, J. S., Lee, C., Pothier, M. A., Farmer, D. K., Martz, T. R., Bertram, T. H., Cappa, C. D., Prather, K. A., and Grassian, V. H.: Acidity across the interface from the ocean surface to sea spray aerosol, *Proc. Natl. Acad. Sci. U.S.A.*, 118, 2, e2018397118, <https://doi.org/10.1073/pnas.2018397118>, 2021.
- Baker, A. R., and Jickells, T. D.: Mineral particle size as a control on aerosol iron solubility, *Geophys. Res. Lett.*, 33, L17608, <https://doi.org/10.1029/2006GL026557>, 2006.
- Baker, A. R., Kanakidou, M., Nenes, A., Myriokefalitakis, S., Croot, P. L., Duce, R. A., Gao, Y., Guieu, C., Ito, A., Jickells, T. D., Mahowald, N. M., Middelburg, R., Perron, M. M. G., Sarin, M. M., Shelley, R., and Turner, D. R.: Changing atmospheric acidity as a modulator of nutrient deposition and ocean biogeochemistry, *Sci. Adv.*, 7, eabd8800, <https://doi.org/10.1126/sciadv.abd8800>, 2021.
- Baker, A. R., Landing, W. M., Bucciarelli, E., Cheize, M., Fietz, S., Hayes, C. T., Kadko, D., Morton, P. L., Rogan, N., Sarthou, G., Shelley, R. U., Shi, Z., Shiller, A., and van Hulst, M. M. P.: Trace element and isotope deposition across the air–sea interface: progress and research needs, *Phil. Trans. R. Soc. A.*, 374, 20160190, <http://dx.doi.org/10.1098/rsta.2016.0190>, 2016.
- Baker, A. R., Li, M., and Chance, R.: Trace metal fractional solubility in size-segregated aerosols from the tropical eastern Atlantic Ocean, *Global Biogeochem. Cy.* 34, e2019GB006510, <https://doi.org/10.1029/2019GB006510>, 2020.
- [Baldo, C., Ito, A., Krom, M. D., Li, W., Jones, T., Drake, N., Ignatyev, K., Davidson, N., and Shi, Z.: Iron from coal combustion particles dissolved much faster than mineral dust under simulated atmospheric acidic condition. *Atmos. Chem. Phys.*, 22, 6045–6066, <https://doi.org/10.5194/acp-22-6045-2022>, 2022.](#)
- Bethke, C. M.: *Geochemical Reaction Modeling: Concepts and Applications*. Oxford University Press, 1996.
- [Bian, Q., Huang, X. H. H., and Yu, J. Z.: One-year observations of size distribution characteristics of major aerosol constituents at a coastal receptor site in Hong Kong – Part 1: Inorganic ions and oxalate. *Atmos. Chem. Phys.*, 14, 9013–9027, <https://doi.org/10.5194/acp-14-9013-2014>, 2014.](#)
- Bibi, I., Singh, B., and Silvester, E.: Dissolution of illite in saline-acidic solutions at 25 °C, *Geochim. Cosmochim. Acta*, 75, 3237–3249, <https://doi.org/10.1016/j.gca.2011.03.022>, 2011.
- Bikkina, P., Kawamura, K., Bikkina, S., Kunwar, B., Tanaka, K., and Suzuki, K.: Hydroxy fatty acids in remote marine aerosols over the Pacific Ocean: Impact of biological activity and wind speed. *ACS Earth Space Chem.*, 3, 366–379, <https://doi.org/10.1021/acsearthspacechem.8b00161>, 2019.
- Bikkina, S., Kawamura, K., and Miyazaki, Y.: Latitudinal distributions of atmospheric dicarboxylic acids, oxocarboxylic acids and α -dicarbonyls over the western North Pacific: sources and formation pathways, *J. Geophys. Res. Atmos.* 120, 5010–5035. <http://dx.doi.org/10.1002/2014JD022235>, 2015.
- Boris, A. J., Lee, T., Pari, T., Choi, J., Seo, S. J., and Collett Jr., J. L.: Fog composition at Baengnyeong Island in the eastern Yellow Sea: detecting markers of aqueous atmospheric oxidations, *Atmos. Chem. Phys.*, 16, 437–453, <https://doi.org/10.5194/acp-16-437-2016>, 2016.
- Boyd, P. W., Jickells, T., Law, C. S., Blain, S., Boyle, E. A., Buesseler, K. O., Coale, K. H., Cullen, J. J., de Beear, H. J. W., Follows, M., Harvey, M., Lancelot, C., Levasseur, M., Owens, N. P. J., Pollard, R., Rivkin, R. B., Sarmiento, J., Schoemann,

- V., Smetacek, V., Takeda, S., Tsuda, A., Turner, S., and Watson, A. J.: Mesoscale iron enrichment experiments 1993–2005: Synthesis, and future directions, *Science*, 315, 612–617, <https://doi.org/10.1126/science.1131669>, 2007.
- 910 Bray, A. W., Oelkers, E. H., Bonneville, S., Wolff-Boenisch, D., Potts, N. J., Fones, G., and Benning, L. G.: The effect of pH, grain size, and organic ligands on biotite weathering rates, *Geochim. Cosmochim. Acta*, 164, 127–145, <http://dx.doi.org/10.1016/j.gca.2015.04.048>, 2015.
- Buck, C. S., Landing, W. M., and Resing, J.: Pacific Ocean aerosols: Deposition and solubility of iron, aluminum, and other trace elements, *Mar. Chem.*, 157, 117–130, <http://dx.doi.org/10.1016/j.marchem.2013.09.005>, 2013.
- 915 Buck, C. S., Landing, W. M., and Resing, J.: Particle size and aerosol iron solubility: A high-resolution analysis of Atlantic aerosols, *Mar. Chem.*, 120, 14–24, <https://doi.org/10.1016/j.marchem.2008.11.002>, 2010.
- Buck, C. S., Landing, W. M., Resing, J. A. and Lebon, G. T.: Aerosol iron and aluminum solubility in the northwest Pacific Ocean: Results from the 2002 IOC cruise, *Geochem. Geophys. Geosyst.*, 7, 4, Q04M07, <https://doi.org/10.1029/2005GC000977>, 2006.
- 920 [Calhoun, J. A., Bates, T. S., and Charlson, R. J.: Sulfur isotope measurements of submicrometer sulfate aerosol particles over the Pacific Ocean. *Geophys. Res. Lett.*, 18, 1877–1880, https://doi.org/10.1029/91GL02304, 1991.](https://doi.org/10.1029/91GL02304)
- Chance, R., Jickells, T. D., and Baker, A. R.: Atmospheric trace metal concentrations, solubility and deposition fluxes in remote marine air over the south-east Atlantic. *Mar. Chem.*, 177, 45–56, <http://dx.doi.org/10.1016/j.marchem.2015.06.028>, 2015.
- 925 Cheize, M., Sarthou, G., Croot, P. L., Bucciarelli, E., Baudoux, A. C., and Baker, A. R.: Iron organic speciation determination in rainwater using cathodic stripping voltammetry, *Anal. Chim., Acta*, 736, <http://dx.doi.org/10.1016/j.aca.2012.05.011>, 45–54, 2012.
- Chen, H., and Grassian, V. H.: Iron dissolution of dust source materials during simulated acidic processing: The effect of sulfuric, acetic, and oxalic acids, *Environ. Sci. Technol.*, 47, 10312–10321, <https://doi.org/10.1021/es401285s>, 2013.
- 930 [Chen, Q., Miyazaki, Y., Kawamura, K., Matsumoto, K., Coburn, S., Volkamer, R., Iwamoto, Y., Kgami, S., Deng, Y., Ogawa, S., Ramasamy, S., Kato, S., Ida, A., Kajii, Y., and Mochida, M.: Characterization of chromophoric water-soluble organic matter in urban, forest, and marine aerosols by HR-ToF-MS analysis and excitation–emission matrix spectroscopy. *Environ. Sci. Technol.*, 50, 10351–10360, https://doi.org/10.1021/acs.est.6b01643, 2016.](https://doi.org/10.1021/acs.est.6b01643)
- [Chung, C. H., You, C. F., Hsu, S. C., Liang, M. C.: Sulfur isotope analysis for representative regional background atmospheric aerosols collected at Mt. Luing, Taiwan. *Sci. Rep.*, 9, 19707, https://doi.org/10.1038/s41598-019-56048-z, 2019.](https://doi.org/10.1038/s41598-019-56048-z)
- 935 Clegg, S. L., Pitzer, K. S., and Brimblecombe, P.: Thermodynamics of multicomponent, miscible, ionic solutions. II. Mixtures including unsymmetrical electrolyte. *J. Phys. Chem.*, 96, 9470–9479, <https://doi.org/10.1021/j100202a074>, 1992.
- Cohcran, R. E., Laskina, O., Hayathane, T., Laskin, A., Laskin, J., Lin, P., Sultana, C., Lee, C., Moore, K. A., Cappa, C. D., Bertram, T. H., Prather, K. A., Grassian, V. H., and Stone, E. A.: Analysis of organic anionic surfactants in fine and coarse fractions of freshly emitted sea spray aerosol, *Environ. Sci. Technol.*, 50, 2477–2486, <https://doi.org/10.1021/acs.est.5b04053>, 2016.
- 940 Conway, T. M., Hamilton D. S., Shelley, R. U., Aguilar-Islas, A. M., Landing, W. M., Mahowald, N. ., and John, S. G.: Tracing and constraining anthropogenic aerosol iron fluxes to the North Atlantic Ocean using iron isotopes, *Nature Commun.*, 10, 2628, <https://doi.org/10.1038/s41467-019-10457-w>, 2019.
- 945 Cwiertny, D. M., Baltrusaitis, J., Hunter, G. J., Laskin, A., Scherer, M. M., and Grassian, V. H.: Characterization and acid-mobilization study of iron-containing mineral dust source materials. *J. Geophys. Res.* 113, D05202, <https://doi.org/10.1029/2007JD009332>, 2008.
- [Deng, C., Brooks, S. D., Vidaurre, G., and Thornton, D. C. O.: Using Raman microspectroscopy to determine chemical composition and mixing state of airborne marine aerosols over the Pacific Ocean. *Aerosol Sci. Technol.*, 48, 193–206, https://doi.org/10.1080/02786826.2013.867297, 2014.](https://doi.org/10.1080/02786826.2013.867297)
- 950 Desboeufs, K. V., Losno, R., Vimeux, F., and Cholbi, S.: The pH-dependent dissolution of wind-transported Saharan dust, *J. Geophys. Res. Atmos.*, 104, D17, 21287–21299, <https://doi.org/10.1029/1999JD900236>, 1999.
- Engelhart, G. J., Hildebrandt, L., Kostenidou, E., Mihalopoulos, N., Donahue, N. M., and Pandis, S. N.: Water content of aged aerosol, *Atmos. Chem. Phys.*, 11, 911–920, <https://doi.org/10.5194/acp-11-911-2011>, 2011.
- 955 [Fang, T., Guo, H., Peltier, R. E., and Weber, R. J. PM_{2.5} water-soluble elements in the southeastern United States: automated analytical method development, spatiotemporal distributions, source apportionment, and implications for health studies. *Atmos. Chem. Phys.*, 15, 11667–11682, https://doi.org/10.5194/acp-15-11667-2015, 2015.](https://doi.org/10.5194/acp-15-11667-2015)

- Fang, T., Guo, H., Zeng, L., Verma, V., Nenes, A., and Weber, R.: Highly Acidic Ambient Particles, Soluble Metals, and Oxidative Potential: A Link between Sulfate and Aerosol Toxicity, *Environ. Sci. Technol.*, 51, 2611–2620, <https://doi.org/10.1021/acs.est.6b06151>, 2017.
- 960 Fitzgerald, E., Ault, A. P., Zauscher, M. D., Mayol-Bracero, O. L., and Prather, K. A.: Comparison of the mixing state of long-range transported Asian and African mineral dust, *Atmos. Environ.*, 115, 19–25, <https://doi.org/10.1016/j.atmosenv.2015.04.031>, 2015.
- Formenti, P., Schüz, L., Balkanski, Y., Desbois, K., Ebert, M., Kandler, K., Petzold, A., Scheuven, D., Weinbruch, S., and Zhang, D.: Recent progress in understanding physical and chemical properties of African and Asian mineral dust. *Atmos. Chem. Phys.*, 11, 8231–8256, <https://doi.org/10.5194/acp-11-8231-2011>, 2011.
- 965 Friese, E., and Ebel, A.: Temperature dependent thermodynamic model of the system $H^+ - NH_4^+ - Na^+ - SO_4^{2-} - NO_3^- - Cl^- - H_2O$. *J. Phys. Chem. A*, 114, 11595–11631, <https://doi.org/10.1021/jp101041j>, 2010.
- Gledhill, M., and Buck, K. N.: The organic complexation of iron in the marine environment: a review. *Front. Microbiol.*, 3, 69, <https://doi.org/10.3389/fmicb.2012.00069>, 2012.
- 970 Graber, E. R., and Rudich, Y.: Atmospheric HULIS: How humic-like are they? A comprehensive and critical review. *Atmos. Chem. Phys.*, 6, 729–753, <https://doi.org/10.5194/acp-6-729-2006>, 2006.
- Guo, H., Nenes, A., and Weber, R. J.: The underappreciated role of nonvolatile cations in aerosol ammonium-sulfate molar ratios, *Atmos. Chem. Phys.*, 18, 17307–17323, <https://doi.org/10.5194/acp-18-17307-2018>, 2018.
- 975 Guo, J., Lou, M., Miao, Y., Wang, Y., Zeng, Z., Liu, H., He, J., Xu, H., Wang, F., Min, M., and Zhai, P. Trans-Pacific transport of dust aerosols from East Asia: Insights gained from multiple observations and modeling. *Environ. Pollut.*, 230, 1030–1039, <https://doi.org/10.1016/j.envpol.2017.07.062>, 2017.
- Hagvall, K., Persson, P., and Karlsson, T.: Speciation of aluminum in soils and stream waters: The importance of organic matter, *Chem. Geol.*, 417, 32–43, <http://dx.doi.org/10.1016/j.chemgeo.2015.09.012>, 2015.
- 980 Hamilton, D. S., Scanza, R. A., Feng, Y., Guinness, J., Kok, J. F., Li, L., Liu, X., Rathod, S. D., Wan, J. S., Wu, M., and Mahowald, N. M.: Improved methodologies for Earth system modelling of atmospheric soluble iron and observation comparisons using the Mechanism of Intermediate complexity for Modelling Iron (MIMI v1.0), *Geosci. Model Dev.*, 12, 3835–3862, <https://doi.org/10.5194/gmd-12-3835-2019>, 2019.
- Herrmann, H., Schaefer, T., Tilgner, A., Styler, S. A., Weller, C., Teich, M., and Otto, T.: Tropospheric aqueous-phase chemistry: Kinetics, mechanisms, and its coupling to changing gas phase, *Chem. Rev.*, 115, 4259–4334, <https://doi.org/10.1021/cr500447k>, 2015.
- 985 Hsieh, C. C., Chen, H. Y., and Ho, T. Y.: The effect of aerosol size on Fe solubility and deposition flux: A case study in the East China Sea. *Mar. Chem.*, 241, 104106, <https://doi.org/10.1016/j.marchem.2022.104106>, 2022.
- Ildefonse, P., Cabaret, D., Saintavit, P., Calas, G., Flank, A. M., and Lagarde, P.: Aluminum X-ray absorption near edge structure in model compounds and Earth's surface minerals, *Phys. Chem. Minerals*, 25, 112–121, <https://doi.org/10.1007/s002690050093>, 1998.
- 990 Inomata, Y., Ohizumi, T., Take, N., Sato, K., Nishikawa, M.: Transboundary transport of anthropogenic sulfur $PM_{2.5}$ at a coastal site in the Sea of Japan as studied by sulfur isotopic ratio measurement. *Sci. Total. Environ.*, 553, 617–625, <https://doi.org/10.1016/j.scitotenv.2016.02.139>, 2016.
- Ito, A., and Shi, Z.: Delivery of anthropogenic bioavailable iron from mineral dust and combustion aerosols to the ocean, *Atmos. Chem. Phys.*, 16, 85–99, <https://doi.org/10.5194/acp-16-85-2016>, 2016.
- 995 Ito, A.: Atmospheric processing of combustion aerosols as source of bioavailable iron, *Environ. Sci. Technol., Lett.*, 2, 70–75, <https://doi.org/10.1021/acs.estlett.5b00007>, 2015.
- Jeong, G. J., and Nousiainen, T.: TEM analysis of the internal structures and mineralogy of Asian dust particles and the implications for optical modeling, *Atmos. Chem. Phys.* 14, 7233–7254, <https://doi.org/10.5194/acp-14-7233-2014>, 2014.
- 1000 Jickells, T. D., An, Z. S., Andersen, K. K., Baker, A. R., Bergametti, G., Brooks, N., Cao, J. J., Boyd, P. W., Duce, R. A., Hunter, K. A., Kawahata, H., Kubilay, N., laRoche, J., Liss, P. S., Mahowald, N., Prospero, J. M., Ridgwell, A. J., Tegen, I., and Torres, R.: Global iron connections between desert dust, ocean biogeochemistry, and climate. *Science*, 308, 67–71, <https://doi.org/10.1126/science.1105959>, 2005.
- 1005 Kawamura, K and Bikina, S: A review of dicarboxylic acids and related compounds in atmospheric aerosols: Molecular distributions, sources, and transformation, *Atmos. Res.*, 170, 140–160, <http://dx.doi.org/10.1016/j.atmosres.2015.11.018>, 2016.

- Kim, H. J., Lee, T., Park, T., Park, G., Collett Jr., J. L., Park, K., Ahn, J. Y., Ban, J., Kang, S., Kim, K., Park, S. M., Jho, E. H., and Choi, Y.: Ship-borne observations of sea fog and rain chemistry over the North and South Pacific Ocean, *J. Atmos. Chem.* 76, 315–326, <https://doi.org/10.1007/s10874-020-09403-8>, 2019.
- 010 [Knadler, K., Lieke, K., Benker, N., Emmel, C., Küpper, M., Müller-Ebert, D., Ebert, M., Scheuvs, D., Sciaditz, A., Schütz, L., Weinbrunch, S.: Electron microscopy of particles collected at Praia, Cape Verde, during the Saharan mineral dust experiment: particle chemistry, shape, mixing state and complex refractive index. *Tellus B*, 63, 475–496, <https://doi.org/10.1111/j.1600-0889.2011.00550.x>, 2017.](https://doi.org/10.1111/j.1600-0889.2011.00550.x)
- 015 [Knopf, D. A., Charnawskas, J. C., Wang, P., Wong, B., Tomlin, J. M., Jankowski, K. A., Fraund, M., Veghte, D. P., China, S., Laskin, A., Moffet, R. C., Gilles, M. K., Aller, J. Y., Marcus, M. A., Raveh-Rubin, S., and Wang, J.: Micro-spectroscopic and freezing characterization of ice-nucleating particles collected in the marine boundary layer in the eastern North Atlantic. *Atmos. Chem. Phys.*, 22, 5377–5398, <https://doi.org/10.5194/acp-22-5377-2022>, 2022.](https://doi.org/10.5194/acp-22-5377-2022)
- Kurusu, M., Adachi, K., Sakata, K., and Takahashi, Y.: Stable isotope ratios of combustion iron produced by evaporation in a steel plant, *ACS Earth Space Chem.*, 3, 588–598, <https://doi.org/10.1021/acsearthspacechem.8b00171>, 2019.
- 020 Kurusu, M., Sakata, K., Uematsu, M., Ito, A., and Takahashi, Y.: Contribution of combustion Fe in marine aerosols over the northwestern Pacific estimated by Fe stable isotope ratios, *Atmos. Chem. Phys.*, 21, 16027–16050, <https://doi.org/10.5194/acp-21-16027-2021>, 2021.
- Kurusu, M., Takahashi, Y., Iizuka, T., and Uematsu, M.: Very low isotope ratio of iron in fine aerosols related to its contribution to the surface ocean, *J. Geophys. Res. Atmos.*, 121, 11119–11136, <https://doi.org/10.1002/2016JD024957>, 2016.
- 025 [Li, J., Michalski, G., Davy, P., Harvey, M., Katzman, T., Wilkins, B.: Investigating source contributions of size-aggregated aerosols collected in Southern Ocean and Baring Head, New Zealand using sulfur isotopes, *Geophys. Res. Lett.*, 45, 3717–3727, <https://doi.org/10.1002/2018GL077353>, 2018.](https://doi.org/10.1002/2018GL077353)
- [Li, W., and Shao, L.: Transmission electron microscopy study of aerosol particles from the brown hazes in northern China, *J. Geophys. Res. Atmos.*, 114, D09302, <https://doi.org/10.1029/2008JD011285>, 2009.](https://doi.org/10.1029/2008JD011285)
- 030 [Li, W., Xu, L., Liu, X., Zhang, J., Lin, Y., Yao, X., Gao, H., Zhang, D., Chen, J., Wang, W., Harrison, R. M., Zhang, X., Shao, L., Fu, P., Nenes, A., and Shi, Z.: Air pollution-aerosol interactions produce more bioavailable iron for ocean ecosystems. *Sci. Adv.*, 3, e1601749, <https://doi.org/10.1126/sciadv.1601749>, 2017.](https://doi.org/10.1126/sciadv.1601749)
- Longo, A. F., Feng, Y., Lai, B., Landing, W. M., Shelley, R. U., Nenes, A., Mihalopoulos, N., Violaki, K., and Ingall, E. D.: Influence of atmospheric processes on the solubility and composition of iron in Saharan dust, *Environ. Sci. Technol.*, 50, 6912–6920, <https://doi.org/10.1021/acs.est.6b02605>, 2016.
- 035 Mackie, D. S., Boyd, P. W., Hunter, K. A., and McTainsh, G. H.: Simulating the cloud processing of iron in Australian dust: pH and dust concentration, *Geophys. Res. Lett.*, 32, L06809, <https://doi.org/10.1029/2004GL022122>, 2005.
- Mahowald, N. M., Hamilton, D. S., Mackey, K. R. M., Moore, J. K., Baker, A. R., Scanza, R. A. and Zhang, Y.: Aerosol trace metal leaching and impacts on marine microorganisms, *Nat. Commun.*, 9(1), 1–15, <https://doi.org/10.1038/s41467-018-04970-7>, 2018.
- 040 Martin, J. H., and Fitzwater, S. E.: Iron deficiency limits phytoplankton growth in the north-west Pacific subarctic, *Nature*, 331, 341–343, <https://doi.org/10.1126/science.1105959>, 1988.
- Maters, E. C., Delmelle, P., and Bonneville, S.: Atmospheric processing of volcanic glass: Effects on iron solubility and redox speciation, *Environ. Sci. Technol.*, 50, 5033–5040, <https://doi.org/10.1021/acs.est.5b06281>, 2016.
- 045 [Matsuki, A., Iwasaka, Y., Shi, G., Zhang, D., Trochkin, D., Yamada, M., Kim, Y. S., Chen, B., Nagatani, T., Miyazawa, T., Nagatani, M., and Nakata, H.: Morphological and chemical modification of mineral dust: Observational insight into the heterogeneous uptake of acidic gases, *Geophys. Res. Lett.*, 32, L22806, <https://doi.org/10.1029/2005GL024176>, 2005.](https://doi.org/10.1029/2005GL024176)
- Mekhidze, N., Völker, C.: Al-Abadleh, H. A., Barbeau, K., Bressac, M., Buck, C., Bundy, R. M., Croot, P., Feng, Y., Ito, A., Johansen, A. M., Landing, W. M., Mao, J., Myriokefalitakis, S., Ohnemus, D., Pasquier, B., and Ye, Y.: Perspective on identifying and characterizing the process controlling iron speciation and residence time at the atmosphere-ocean interface, *Mar. Chem.*, 217, 103704, <https://doi.org/10.1016/j.marchem.2019.103704>, 2019.
- 050 Meskhidze, N., Hurley, D., Royalty, T. M., and Johnson, M. S.: Potential effect of atmospheric dissolved organic carbon on the iron solubility in seawater, *Mar. Chem.*, 194, 124–132, <http://dx.doi.org/10.1016/j.marchem.2017.05.011>, 2017.
- 055 [Miyamoto, C., Sakata, K., Yamakawa, Y., and Takahashi, Y.: Determination of calcium and sulfate species in aerosols associated with the conversion of its species through reaction processes in the atmosphere and its influence on cloud condensation nucleation. *Atmos. Environ.*, 223, 117193, <https://doi.org/10.1016/j.atmosenv.2019.117193>, 2020.](https://doi.org/10.1016/j.atmosenv.2019.117193)

- Mochida, M., Kitamori, Y., and Kawamura, K.: Fatty acids in the marine atmosphere: Factors governing their concentrations and evaluation of organic films on sea-salt particles, *J. Geophys. Res.*, 107, D17, 4325, <https://doi.org/10.1029/2001JD001278>, 2002.
- 060 Moffet, R. C., Furutani, H., Rödel, T. C., Henn, T. R., Sprau, P. O., Laskin, A., Uematsu, M., and Gilles, M. K.: Iron speciation and mixing in single aerosols particles from the Asian continental outflow, *J. Geophys. Res.*, 117, D07204, <https://doi.org/10.1029/2011JD016746>, 2012.
- Moore, C. M., Mills, M. M., Arrigo, K. R., Berman-Frank, I., Bopp, L., Boyd, P. W., Galbraith, E. D., Geider, R. J., Guieu, C., Jaccard, S. L., Jickells, T. D., La Roche, J., Lenton, T. M., Mahowald, N. M., Marañón, E., Marinov, I., Moore, J. K., 065 Nakatsuka, T., Oeschies, A., Saito, M. A., Thingsted, T. F., Tsuda, A., and Ulloa, O.: Processes and patterns of oceanic nutrient limitation, *Nature Geosci.*, 6, 701–710, <https://doi.org/10.1038/ngeo1765>, 2013.
- Mori, I., Sun, Z., Ukachi, M., Nagano, K., McLeod, C. Q., Cox, A. G., Nishikawa, M.: Development and certification of the new NIES CRM 28: urban aerosols for the determination of multielements, *Anal. Bioanal. Chem.*, 391, 1997–2003, <https://doi.org/10.1007/s00216-008-2076-y>, 2008.
- 070 Nault, B. A., Campuzano-Jost, P., Day, D. A., Jo, D. S., Schroder, J. C., Allen, H. M., Bahreini, R., Bian, H., Blake, D. R., Chin, M., Clegg, S. L., Colarco, P. R., Crouse, J. D., Cubison, M. J., DeCarlo, P. F., Dibb, J. E., Diskin, G. S., Hodzic, A., Hu, W., Katich, J. M., Kim, M. J., Kodros, J. K., Kupc, A., Lopez-Hilfiker, F. D., Marais, E., Middlebrook, A. M., Neuman, J. A., Nowak, J. B., Palm, B. B., Paulot, F., Pierce, J. R., Schill, G. P., Scheuer, E., Thornton, J. A., Tsigaridis, K., Wennberg, P. O., Williamson, C. J., and Jimenez, J. L.: Chemical transport models often underestimate inorganic aerosol acidity in 075 remote regions of the atmosphere, *Commun. Earth Environ.*, 2, 93, <https://doi.org/10.1038/s43247-021-00164-0>, 2021.
- Nomura, M., and Koyama, A.: Performance of beamline with a pair of bent conical mirrors, *Nucl. Instrum. Methods Phys. Res. A.*, 467–468, 733–736, [https://doi.org/10.1016/S0168-9002\(01\)00482-X](https://doi.org/10.1016/S0168-9002(01)00482-X), 2001.
- Nriagu, J. O., and Pacyna, J. M.: Quantitative assessment of worldwide contamination of air, water and soils by trace metals, *Nature*, 333, 134–139, <https://doi.org/10.1038/333134a0>, 1988.
- 080 Oakes, M., Weber, R. J., Lai, B., Russell, A., and Ingall, E.: Characterization of iron speciation in urban and rural single particles using XANES spectroscopy and micro X-ray fluorescence measurements: investigating the relationship between speciation and fractional iron solubility, *Atmos. Chem. Phys.*, 12, 745–756, <https://doi.org/10.5194/acp-12-745-2012>, 2012.
- Paris, R., and Desboeufs, K. V.: Effect of atmospheric organic complexation on iron-bearing dust solubility, *Atmos. Chem. Phys.*, 13, 4895–4905, <https://doi.org/10.5194/acp-13-4895-2013>, 2013.
- 085 Paulot, F., Jacob, D. J., Johnson, M. T., Bell, T. G., Baker, A. R., Keene, W. C., Lima, I. D., Doney, S. C., and Stock, C. A.: Global oceanic emission of ammonia: Constraints from seawater and atmospheric observations, *Global Biogeochem. Cy.*, 29, 1165–1178, <https://doi.org/10.1002/2015GB005106>, 2015.
- Prather, K. A., Bertram, T. H., Grassian, V. H., Deane, G. B., Stokes, M. D., DeMott, P. J., Aluwihare, L. I., Palenik, B. P., Azam, F., Seinfeld, J. H., Moffet, R. C., Molina, M. J., Cappa, C. D., Geiger, F. M., Roberts, G. C., Russell, L. M., Ault, A. P., Baltusaitis, J., Collings, D. B., Corrigan, C. E., Cuadra-Rodriguez, L. A., Ebben, C. J., Forestieri, S. D., Guasco, T. J., Hersey, S. P., Kim, M. J., Lambert, W. F., Modini, R. L., Mui, W., Pedler, B. E., Ruppel, M. J., Ryder, O. S., Schoepp, N. G., Sullivan, R. C., and Zhao, D.: Bringing the ocean into the laboratory to probe the chemical complexity of sea spray aerosol. *Proc. Natl. Acad. Sci. U.S.A.*, 110, 7550–7555, <https://doi.org/10.1073/pnas.1300262110>, 2013.
- 090 [Pruppacher, H. R., and Jaenicke, R. The processing of water vapor and aerosols by atmospheric clouds, a global estimate. *Atmos. Res.*, \[https://doi.org/10.1016/0169-8095\\(94\\)00098-X\]\(https://doi.org/10.1016/0169-8095\(94\)00098-X\), 28, 283–295, 1995.](https://doi.org/10.1016/0169-8095(94)00098-X)
- 095 Sakata, K., Kurisu, M., Tanimoto, H., Sakaguchi, A., Uematsu, M., Miyamoto, C., and Takahashi, Y.: Custom-made PTFE filters for ultra-clean size-fractionated aerosol sampling for trace metals, *Mar. Chem.*, 206, 100–108, <https://doi.org/10.1016/j.marchem.2018.09.009>, 2018.
- 100 Sakata, K., Sakaguchi, A., Tanimizu, M., Takaku, Y., Yokoyama, Y., and Takahashi, Y.: Identification of sources of lead in the atmosphere using X-ray absorption near-edge structure (XANES) spectroscopy, *J. Environ. Sci.*, 26, 343–352, [https://doi.org/10.1016/S1001-0742\(13\)60430-1](https://doi.org/10.1016/S1001-0742(13)60430-1), 2014.
- Sakata, K., Takahashi, Y., Takano, S., Matsuki, A., Sakaguchi, A., Tanimoto, H.: First X-ray spectroscopic observations of atmospheric titanium species: size dependence and the emission source, *Environ. Sci. Technol.*, 55, 10975–10986, <https://doi.org/10.1021/acs.est.1c02000>, 2021.

- 105 Sakata, M., Kurata, M., and Tanaka, N.: Estimating contribution from municipal solid waste incineration to trace metal concentrations in Japanese urban atmosphere using lead as a marker element, *Geochem. J.*, 34, 23–32, <https://doi.org/10.2343/geochemj.34.23>, 2000.
- Salazar, J. R., Pfothenhauer, D. J., Leresche, F., Rosario-Ortiz, F. L., Hannigan, M. P., Fakra, S. C., & Majestic, B. J.: Iron speciation in PM_{2.5} from urban, agriculture, and mixed environments in Colorado, USA. *Earth and Space Sci.*, 7, e2020EA001262, <https://doi.org/10.1029/2020EA001262>, 2020.
- 110 Salma, I., and Láng, G. G.: How many carboxyl groups does an average molecule of humic-like substances contain?, *Atmos. Chem. Phys.*, 8, 5997–6002, <https://doi.org/10.5194/acp-8-5997-2008>, 2008.
- Sambutoba, V., Didenko, T., Kunenkov, E., Emmenegger, C., Zenobi, R., and Kalbere, M.: Functional group analysis of high-molecular weight compounds in the water-soluble fraction of organic aerosols, *Atmos. Environ.*, 41, 4703–4710, <https://doi.org/10.1016/j.atmosenv.2007.03.033>, 2007.
- 115 [Santander, M. V., Mitts, B. A., Pendergraft, M. A., Dinasquet, J., Lee, C., Moore, A. N., Cancelada, L. B., Kimble, K. A., Malfatti, F., Prather, K. A.: Tandem fluorescence measurements of organic matter and bacteria released in sea spray aerosols. *Environ. Sci. Technol.*, 55, 5171–5179, <https://doi.org/10.1021/acs.est.0c05493>, 2021.](https://doi.org/10.1021/acs.est.0c05493)
- Schlitzer, R.: Ocean Data View, odv.awi.de, 2021.
- 120 Schroth, A. W., Crusius, J., Sholkovitz, E. R., and Bostick, B. C.: Iron solubility driven by speciation in dust sources to the ocean, *Nature Geosci.*, 2, 337–340, <https://doi.org/10.1038/ngeo501>, 2009.
- Sedwick, P. N., Sholkovitz, E. R., and Chirch, T. M.: Impact of anthropogenic combustion emissions on the fractional solubility of aerosol iron: Evidence from the Sargasso Sea, *Geochem. Geophys. Geosyst.*, 8, 10, Q10Q06, <https://doi.org/10.1029/2007GC001586>, 2007.
- 125 Shah, V., Jacob, D. J., Moch, J. M., Wang, X., and Zhai, S.: Global modelling of cloud water acidity, precipitation acidity, and acid inputs to ecosystem, *Atmos. Chem. Phys.* 20, <https://doi.org/10.5194/acp-20-12223-2020>, 12223–12245, 2020.
- Shaw, S. A., Peak, D., Hendry, M. J.: Investigation of acidic dissolution of mixed clays between pH 1.0 and -3.0 using Si and Al X-ray absorption near edge structure, *Geochim. Cosmochim. Acta*, 73, 4151–4165, <https://doi.org/10.1016/j.gca.2009.04.004>, 2009.
- 130 [Shelley, R. U., Landing, W. M., Ussher, S. J., Planquette, H., and Sarthou, G.: Regional trends in the fractional solubility of Fe and other metals from North Atlantic aerosols \(GEOTRACES cruises GA01 and GA03\) following a two-stage leach. *Biogeosci.*, 15, 2271–2288, <https://doi.org/10.5194/bg-15-2271-2018>, 2018.](https://doi.org/10.5194/bg-15-2271-2018)
- Shi, Z., Bonneville, S., Krom, M. D., Carslaw, K. S., Jickells, T. D., Baker, A. R., and Benning, L. G.: Iron dissolution kinetics of mineral dust at low pH during simulated atmospheric processing, *Atmos. Chem. Phys.*, 11, 995–1007, <https://doi.org/10.5194/acp-11-995-2011>, 2011.
- 135 Shi, Z., Krom, M. D., and Bonneville, S.: Formation of iron nanoparticles and increases in iron reactivity in mineral dust during simulated cloud processing, *Environ. Sci. Technol.*, 43, 6592–6596, <https://doi.org/10.1021/es901294g>, 2009.
- Shi, Z., Krom, M. D., Bonneville, S., and Benning, L. G.: Atmospheric processing outside clouds increases soluble iron in mineral dust, *Environ. Sci. Technol.*, 49, 1472–1477, <https://doi.org/10.1021/es504623x>, 2015.
- 140 Sholkovitz, E. R., Sedwick, P. N., and Chirch, T. M.: Influence of anthropogenic combustion emissions on the deposition of soluble aerosol iron to the ocean: Empirical estimates for island sites in the North Atlantic, *Geochim. Cosmochim. Acta*, 73, 14, 3981–4003, <https://doi.org/10.1016/j.gca.2009.04.029>, 2009.
- Spokes, L., Jickells, T. D., and Lim, B.: Solubilisation of aerosol trace metals by cloud processing: A laboratory study, *Geochim. Cosmochim. Acta*, 58, 15, 3281–3287, [https://doi.org/10.1016/0016-7037\(94\)90056-6](https://doi.org/10.1016/0016-7037(94)90056-6), 1994.
- 145 [Spranger, T., van Pinxteren, D., and Herrman, H.: Atmospheric “HULIS” in different environments: Polarities, molecular sizes, and sources suggest more than 50% are not “humic-like”. *ACS Earth Space Chem.*, 4, 272–282, <https://dx.doi.org/10.1021/acsearthspacechem.9b00299>, 2020.](https://doi.org/10.1021/acsearthspacechem.9b00299)
- Stein, A. F., Draxler, R. R., Rolph, G. D., Stunder, B. J. B., Cohen, M. D. and Ngan, F.: NOAA’s hysplit atmospheric transport and dispersion modeling system, *Bull. Am. Meteorol. Soc.*, 96(February), 2059–2077, <https://doi.org/10.1175/BAMS-D-14-00110.1>, 2015.
- 150 [Straub, D. J., Lee, T., Collett, J. L.: Chemical composition of marine stratocumulus clouds over the eastern Pacific Ocean. *J. Geophys. Res. Atmos.* 112, D04307, <https://doi.org/10.1029/2006JD007439>, 2007.](https://doi.org/10.1029/2006JD007439)
- Sullivan, R. C., Guazzotti, S. A., Sodeman, D. A., and Prather, K. A.: Direct observations of the atmospheric processing of Asian mineral dust, *Atmos. Chem. Phys.*, 7, 1213–1236, <https://doi.org/10.5194/acp-7-1213-2007>, 2007.

- 155 Sullivan, T. S., Ramkissoon, S., Garrison, V. H., Ramsubhag, A., and Thies, J. E.: Siderohore production of African dust microorganisms over Trinidad and Tobago, *Aerobiologia*, 28, 391–401, <https://doi.org/10.1007/s10453-011-9243-x>, 2012.
- Takahashi, Y., Furukawa, T., Kanai, Y., Uematsu, M., Zheng, G., and Marcus, M. A.: Seasonal changes in Fe species and soluble Fe concentration in the atmosphere in the Northwest Pacific region based on the analysis of aerosols collected in Tsukuba, Japan, *Atmos. Chem. Phys.*, 13, 7695–7710, <https://doi.org/10.5194/acp-13-7695-2013>, 2013.
- 160 Takahashi, Y., Higashi, M., Furukawa, T., and Mitsunobu, S.: Change of iron species and iron solubility in Asian dust during the long-range transport from western China to Japan, *Atmos. Chem. Phys.*, 11, 11237–11252, <https://doi.org/10.5194/acp-11-11237-2011>, 2011.
- [Takahashi, Y., Miyoshi, T., Yabuki, S., Inada, Y., and Shimizu, H.: Observation of transformation of calcite to gypsum in mineral aerosols by Ca K-edge X-ray absorption near-edge structure \(XANES\). *Atmos. Environ.*, 42, 6535–6541, <https://doi.org/10.1016/j.atmosenv.2008.04.012>, 2008.](https://doi.org/10.1016/j.atmosenv.2008.04.012)
- 165 Takeichi, Y., Inami, N., Suga, H., Miyamoto, C., Ueno, T., Mases, K., Takahashi, Y., and Ono, K.: Design and performance of a compact scanning transmission X-ray microscope at the Photon Factory, *Rev. Sci. Instrum.*, 87, 013704, <http://dx.doi.org/10.1063/1.4940409>, 2016.
- Tao, Y., and Murphy, J. G.: The mechanisms responsible for the interactions among oxalate, pH and Fe dissolution in PM_{2.5}, *ACS Earth Space Chem.*, 3, 2259–2265, <https://doi.org/10.1021/acsearthspacechem.9b00172>, 2019.
- 170 Taylor, S. R.: Abundance of chemical elements in the continental crust: a new table, [https://doi.org/10.1016/0016-7037\(64\)90129-2](https://doi.org/10.1016/0016-7037(64)90129-2), *Geochim. Cosmochim. Acta*, 28, 1273–1285, 1964.
- Vinatier, V., Wirgot, N., Joly, M., Sancelme, M., Abrantes, M., Deguillaume, L., and Delort, A. M.: Sidreophore in cloud waters and potential impact on atmospheric chemistry: Production by microorganisms isolated at the Puy de Dôme station, *Environ. Sci. Technol.*, 50, 9315–9323, <https://doi.org/10.1021/acs.est.6b02335>, 2016.
- 175 [Wagner, T., Guieu, C., Losno, R., Bonnet, S., and Mahowald, N.: Revisiting atmospheric dust export to the Southern Hemisphere ocean: biogeochemical implications. *Global Biogeochem. Cy.*, 22, GB2006, <https://doi.org/10.1029/2007GB002984>, 2008.](https://doi.org/10.1029/2007GB002984)
- 180 Wang, Z., Fu, H., Zhang, L., Song, W., and Chen, J.: Ligand-promoted photoreductive dissolution of goethite by atmospheric low-molecular dicarboxylates, *J. Phys. Chem. A*, 121, 1647–1656, <https://doi.org/10.1021/acs.jpca.6b09160>, 2017.
- Wilson, T. W., Ladino, L. A., Alpert, P. A., Breckels, M. N., Brooks, I. M., Browse, J., Burrows, S. M., Carslaw, K. S., Huffman, J. A., Judd, C., Kilhau, W. P., Mason, R. H., McFiggans, G., Miller, L. A., Nájera, J. J., Polishchuk, E., Rae, S., Schiller, C. L., Si, M., Temprado, J. V., Whale, T. F., Wong, J. P. S., Wurl, O., Yakobi-Hancock, J. D., Abbatt, J. P. D.,
- 185 Aller, J. Y., Bertram, A. K., Knopf, D. A., and Murray, B. J.: A marine biogenic source of atmospheric ice-nucleating particles, *Nature*, 525, 234–238, <https://doi.org/10.1038/nature14986>, 2015.
- [Wong, J. P. S., Yang, Y., Fang, T., Mulholland, J. A., Russell, A. G., Ebel, S., Nenes, A., Weber, R. J. Fine particle iron in soils and road dust is modulated by coal-fired power plant sulfur. *Environ. Sci. Technol.*, 54, 7088–7096, <https://dx.doi.org/10.1021/acs.est.0c00483>, 2020.](https://dx.doi.org/10.1021/acs.est.0c00483)
- 190 Wozniak, A. S., Shelley, R. U., McElhenie, S. D., Landing, W. M., and Hatcher, P. G.: Aerosol water soluble organic matter characteristics over the North Atlantic Ocean: Implications for iron-binding ligands and iron solubility, *Mar. Chem.*, 173, 162–172, <http://dx.doi.org/10.1016/j.marchem.2014.11.002>, 2015.
- Wozniak, A. S., Shelley, R. U., Sleighter, R. L., Abdulla, H. A. N., Morton, P. L., Landing, W. M., and Hatcher, P. G.: Relationships among aerosol water soluble organic matter, iron and aluminum in European, North African, and marine air masses from the 2010 US GEOTRACES cruise, *Mar. Chem.*, 154, 24–33, <http://dx.doi.org/10.1016/j.marchem.2013.04.011>, 2013.
- 195 [Yao, X., Fang, M., Chan, C. K.: Size distributions and formation of dicarboxylic acids in atmospheric particles. *Atmos. Environ.*, 36, 2099–2107, \[https://doi.org/10.1016/S1352-2310\\(02\\)00230-3\]\(https://doi.org/10.1016/S1352-2310\(02\)00230-3\), 2002.](https://doi.org/10.1016/S1352-2310(02)00230-3)
- [Zhang, H., Li, R., Dong, S., Wang, F., Zhu, Y., Meng, H., Huang, C., Ren, Y., Wang, X., Hu, X., Li, T., Peng, C., Zhang, G., Xue, L., Wang, X., and Tang, M.: Abundance and fractional solubility of aerosol iron during winter at a coastal city in northern China: Similarities and contrasts between fine and coarse particles. *J. Geophys. Res. Atmos.*, 127, e2021JD036070, <https://doi.org/10.1029/2021JD036070>, 2022.](https://doi.org/10.1029/2021JD036070)
- 200